Incident shock Mach number effects on Richtmyer-Meshkov mixing in a heavy gas layer

G. C. Orlicz,[1] S. Balasubramanian,[2] and K. P. Prestridge[1,a]

[1]*Extreme Fluids Team, P-23, Physics Division, Los Alamos National Laboratory, Los Alamos, New Mexico 87545, USA*
[2]*Department of Mechanical Engineering, Indian Institute of Technology, Bombay, Mumbai, Maharashtra 400076, India*

Experiments were performed at the horizontal shock tube facility at Los Alamos National Laboratory to study the effect of incident shock Mach number (M) on the development of Richtmyer-Meshkov instability after a shock wave impulsively accelerates a varicose-perturbed, heavy-gas curtain. Three cases of incident shock strength were experimentally investigated: $M = 1.21$, 1.36, and 1.50. We discuss the state of the mixing and the mechanisms that drive the mixing at both large and small scales by examining the time evolution of 2D density fields derived from quantitative planar laser-induced fluorescence measurements. Several differences in qualitative flow features are identified as a result of Mach number variation, and differences in vortex interaction, observed using particle image velocimetry, play a critical role in the development of the flow field. Several quantities, including mixing layer width, mixing layer area, interface length, instantaneous mixing rate, the density self-correlation parameter, probability density functions of the density field, and mixing progress variables are examined as a function of time. These quantities are also examined versus time scaled with the convection velocity of the mixing layer. A higher incident Mach number yields greater mixing uniformity at a given downstream location, while a lower Mach number produces a greater amount of total mixing between the two gases, suggesting possible implications for optimization in applications with confined geometries. © *2013 AIP Publishing LLC*.
[http://dx.doi.org/10.1063/1.4827435]

I. INTRODUCTION

The Richtmyer-Meshkov instability (RMI) occurs when a perturbed interface between two fluids of different densities undergoes an impulsive acceleration, such as a shock wave.[1,2] Vorticity is deposited baroclinically along the interface wherever the density and pressure gradients are misaligned, causing stretching of the interface and growth of the initial perturbations. Given enough energy deposition during interaction of the shock wave with the initial conditions, the flow may eventually transition to turbulent mixing. Reviews of RMI can be found in Brouillette[3] and Vorobieff and Kumar.[4]

The RMI plays an important role in the mixing processes in inertial confinement fusion (ICF), supersonic combustion ramjet engines, and supernovae. In ICF, RMI induced mixing results in less fusion yield, and is currently a major hurdle for achieving an efficient fusion power source.[5,6] Conversely, mixing is desired in supersonic combustion ramjet engines where the RMI can be utilized to enhance the degree of mixing between fuel and oxidizer for improved combustion rate and engine efficiency.[7] The RMI also occurs naturally in supernovae where it is responsible for the distribution of heavy elements throughout the universe and features we observe in supernova

a)kpp@lanl.gov. URL: http://www.lanl.gov/projects/shocktube/.

remnants.[8] To improve upon modeling and simulation efforts in shock-driven flows, it is necessary to understand the factors that influence RMI growth and mixing.

For the special case of a single discontinuous interface with single-mode 2D perturbations of sufficiently small amplitude, Richtmyer's linear impulsive model for amplitude growth is generally accepted as valid, with

$$\dot{a} = \kappa A \Delta v a_0, \tag{1}$$

where a is the perturbation amplitude, a_0 is the initial perturbation amplitude, κ is the wavenumber of the perturbations, Δv is the velocity imparted upon the interface by the impulsive acceleration, and the Atwood number is defined as $A = (\rho_2 - \rho_1)/(\rho_2 + \rho_1)$, where ρ_1 and ρ_2 are the densities of the two fluids. Amplitude growth is linear as long as the amplitude is relatively small,[9] usually taken to be $ka < 1$. As the perturbations grow, strong nonlinearities come into play and growth is no longer governed by Eq. (1). Recent work has extended the impulsive 2D model to the more general 3D case and has shown that the 2D model can over-predict early time growth rates if the perturbations are 3D in nature.[10]

Many physical parameters affect RMI growth. The initial interface between the two fluids is often diffuse, resulting in a reduction of the growth rate from Richtmyer's model. The incident shock wave compresses the perturbation amplitude and alters the Atwood number. Refraction of the shock wave as it traverses the interface will change the initial vorticity deposition,[11–14] and reflected shock or rarefaction waves from the interface further complicate modeling efforts.[3] If the interface is accelerated to a velocity, Δv, close to the local speed of sound or close to the velocity of the shock wave, additional compressibility effects have been observed.[13] The effect of these factors on RMI growth and mixing is largely unknown, even for simple single-interface geometries, although a recent model has been developed that accounts for some of these effects and has been shown to predict both early and later time growth for simulations performed over a broad parameter space.[15] Experimental data are required across a broad range of parameters, including incident shock Mach number (M), to improve our understanding of the RMI, and to be able to predict its affect on mixing.

Advanced imaging diagnostics, including quantitative planar laser induced fluorescence (PLIF)[16–18] and particle image velocimetry (PIV),[19] have begun to yield experimental measurements of density and velocity fields that provide a much more rigorous approach to quantifying the mixing processes at a variety of length scales in RMI flows. Recent experimental studies have acquired PLIF and PIV measurements simultaneously.[20,21] Simultaneous measurements of density and velocity are critical for fully characterizing the mixing processes in variable density flows where the dynamic response of the fluid to a stress is coupled to the density. This added dependence introduces new fluid physics to the mixing problem when compared to constant density mixing problems, and is termed level-2 mixing by Dimotakis.[22]

The goal of the present study is to apply state of the art simultaneous PIV and quantitative PLIF imaging diagnostics to investigate the effect of incident shock Mach number on RMI mixing. Previous experimental work investigating Mach number effects has been limited by the amount of data that was acquired and the available diagnostic capability. One experimental study performed quantitative PLIF with $M = 1.1$, 1.2, and 1.3 shock waves and found that growth rates could be collapsed.[23] Another single-interface experiment used a variety of qualitative visualization techniques to study a wide parameter space with $1.1 < M < 3$ (as well as a range of Atwood numbers), and also demonstrated collapse of the amplitude data using an appropriate scaling.[13] In heavy gas bubble experiments[24] carried out at $M = 2.88$, and light gas bubble experiments[12] at $M = 2.95$, both with qualitative visualization, researchers observed flow field features not previously observed in other gas bubble experiments[25] at $M < 1.3$. Heavy gas columns have also been shocked with $M = 1.22$, 1.66, and 2.02 using qualitative visualization to show collapse of width growth rates in scaled time.[26] In heavy gas curtain experiments at $M = 1.21$ and 1.54 qualitative PLIF measurements showed that growth rates could be collapsed similarly, but that measurements of the instantaneous mixing rate did not collapse with the same scaling.[14] This demonstrated that there could be a disparity in the time scale for small vs large scale mixing when Mach number is varied, and provided motivation for the present work.

The current work represents the first time that quantitative density fields and velocity fields have been reported in a RMI experimental study where Mach number is varied, allowing for a more complete and detailed assessment of the different mixing states that are produced. This work represents an extension to that found in Orlicz et al.[14] and employs similar initial conditions: a varicose perturbed thin heavy gas curtain surrounded by atmospheric air. The presence of two closely spaced interfaces in gas curtain geometries adds complexity to the mixing process because the growth on both interfaces is coupled.[14,27] While the bulk of RMI research has focused on single interface configurations that permit comparison to various forms of Eq. (1), study of multi-interface configurations is important for a better understanding of mixing processes in ICF and supernovae where the RMI is generated at more than one interface. In the present study, experiments were conducted at 3 different Mach numbers: $M = 1.21$, 1.36, and 1.50, with density measurements at more than 40 different post-shock times for each Mach number. The test section is also three times longer than that of Orlicz et al.,[14] allowing interrogation of the curtain at a much more advanced mixing state for each Mach number.

In the present study, we focus on the interplay between advective stirring, characterized by stretching and straining of interfaces due to the deposition of vorticity by a shock wave, and molecular diffusion that occurs along those interfaces. When we discuss the amount of mixing in this context, we refer to how diluted the heavy gas layer has become with air due to cumulative diffusion. Particular attention is spent on the time evolution of relevant mixing quantities that can be derived from the density fields to determine the differences in the amount of mixing, the homogeneity of the mixing, and the mechanisms that drive the mixing when Mach number is varied.

II. EXPERIMENTAL FACILITY AND METHODOLOGY

The experiments were performed at the horizontal gas shock tube facility at Los Alamos National Laboratory using a horizontal shock tube with a 7.62 cm square cross section and a total length of approximately 5.3 m. A schematic of the shock tube can be found in Figure 1. The driven, test, and end sections are open to atmosphere (11.5 psi), while the driver is pressurized using nitrogen (N_2) or helium (He) gas. The required driver pressure was experimentally determined to be approximately 22 psi (N_2), 30 psi (He), and 50 psi (He) for Mach 1.21, Mach 1.36, and Mach 1.50, respectively. Incident shock Mach number was chosen to not exceed $M = 1.50$ due to structural limitations of the test section. Helium was used for the higher Mach number experiments to reduce the operating driver pressure. The operation of the facility is the same as previously reported in Orlicz et al.[14] All measurements in the current experiment were acquired before the developing mixing layer encountered either the reflected shock wave from the end wall or the expansion fan from the driver section.

A. Initial conditions

The initial conditions consist of a thin fluid layer of heavy gas with varicose perturbations surrounded by air. The heavy gas is seeded both with acetone vapor and glycol droplets for PLIF and
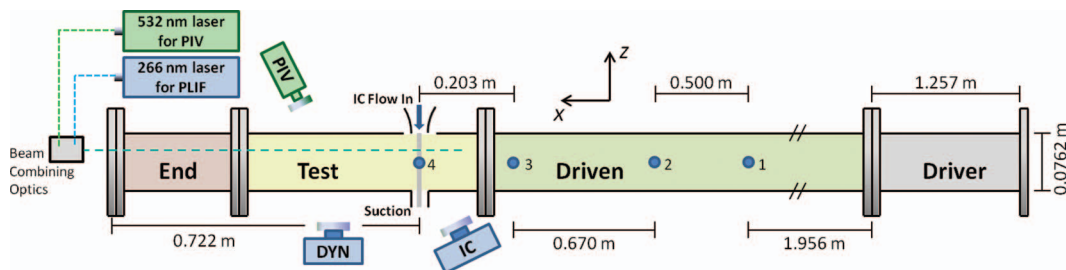

FIG. 1. Shock tube schematic. Diaphragm is placed between Driver and Driven sections. Shock wave travels from right to left, with pressure transducers (PT) labeled 1–4. Shock speed is calculated between PT2 and PT3, and diagnostics are triggered off of PT3, while PT4 is coincident with IC location to measure time of shock interaction.
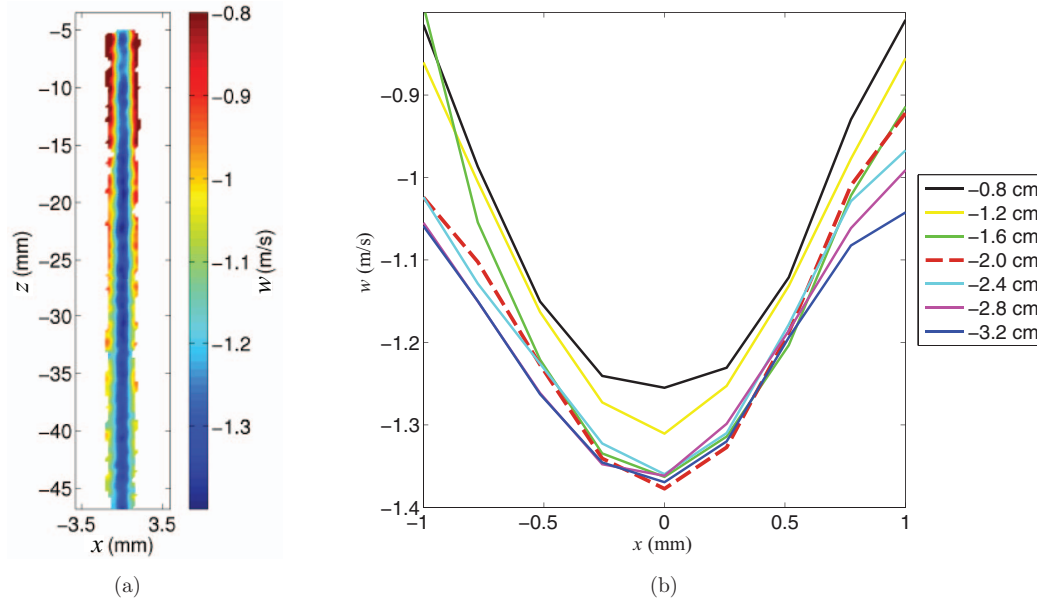
FIG. 2. Initial condition vertical velocity. (a) Spatial map of vertical velocity, w, for initial conditions. $z = 0$ represents the top wall of the shock tube at the nozzle exit. (b) Comparison of streamwise profiles for initial condition vertical velocity, w, at different vertical positions. The red dashed line represents the x-y imaging plane 2 cm below the nozzle exit, with a maximum velocity of 1.38 m/s occurring at the center.

PIV, respectively, before it is introduced into the test section in a manner similar to that of Balakumar et al.[20] The nozzle that creates the perturbations on the interface consists of a row of closely spaced holes of 3 mm diameter and 3.6 mm spacing, and has been described in greater detail in previous work.[14,20]

At the x-y measurement plane (streamwise-spanwise) located 2 cm below the nozzle exit, the maximum vertical flow velocity of the initial conditions was measured to be $w = 1.38$ m/s, as seen in Figures 2(a) and 2(b), which is small compared to the horizontal velocity of the shock-induced flow (>100 m/s for all experiments). The SF_6 concentration along the centerline at the x-y measurement plane is estimated to be $\approx 45\%$ SF_6, with 12% acetone vapor and 43% air by volume. For this composition, the Atwood number is $A = 0.49$, where ρ_1 is the density of air and ρ_2 is the density of the heavy gas mixture at the streamwise center of the curtain. Figures 2(a) and 2(b) were obtained from PIV measurements in the x-z plane aligned with the axis of the center heavy gas cylinder. In the x-y plane, the initial condition concentration profile can be approximated using the expression[20,27]

$$c_v = \frac{C_1(1 + C_2 \cos \kappa y)}{1 + C_2} \exp^{-x^2 \alpha^2 /(1 + \beta \cos \kappa y)^2}, \tag{2}$$

where c_v is the volume fraction of SF_6, and for the current experiment the parameters $C_1 = 0.42$ and $\kappa = 1744$ m^{-1} are the peak concentration and wavenumber of the perturbations, respectively. $C_2 = 0.2$, $\alpha = 836$ m^{-1}, and $\beta = -0.04$ were determined empirically. Using Eq. (2) as a starting point for simulations may be preferable in that it eliminates the random noise in the experimental concentration profiles, as well as other artifacts in the images that result from imperfect image corrections for laser sheet intensity and pixel response. However, it would still be appropriate to add some level of noise to Eq. (2), to more accurately represent the true density profile. Figure 3 compares line profiles and spatial maps of the numerical approximation of the initial conditions to a representative experimental image. Although there is variation of the initial conditions in the vertical (z) direction as the curtain diffuses, the variation is very small compared to the perturbations in the x-y directions, and we consider the initial conditions and the interaction with the incident shock to be 2D.
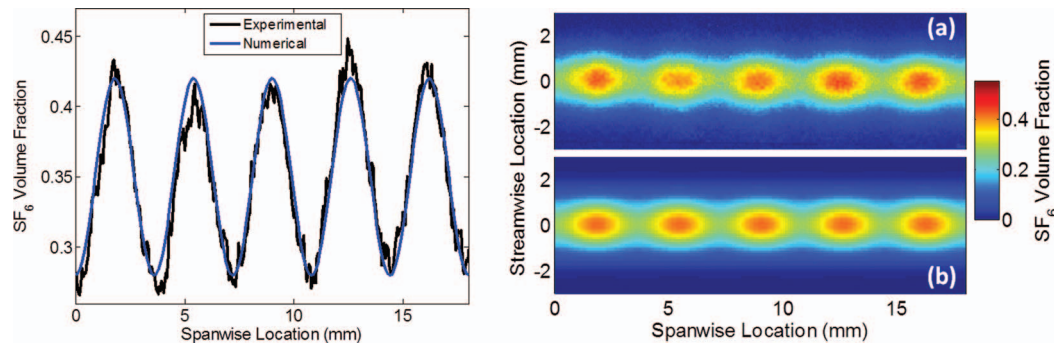
FIG. 3. (Left) Center line profiles of SF_6 volume fraction for an experimental image of the ICs and the numerical representation given in Eq. (2). (Right) Spatial map of SF_6 volume fraction for (a) an experimental IC, and (b) the numerical representation of the ICs using Eq. (2).

B. Imaging diagnostics

All images of the resulting instability were acquired in the x-y plane located 2 cm below the nozzle exit. Two imaging techniques were used simultaneously: PLIF and PIV, although the focus of the current study is on the former. These measurements were made using two dual headed neodymium-doped yttrium aluminum garnet (Nd-YAG) pulsed lasers with output frequencies of 266 nm (frequency quadrupled) for PLIF, and 532 nm (frequency doubled) for PIV. The lasers are co-aligned through a combination of optics and formed into a horizontal laser sheet with a thickness of ~1.5 mm within the measurement region.

The light sheet from the 266 nm PLIF laser causes the acetone vapor to fluoresce within the visible range (350–550 nm), with a peak at 420 nm. The acetone vapor tracks the SF_6 at a molecular level, and the fluorescence was measured to be linear with laser power. Therefore, the resulting images of fluorescence intensity scale linearly with SF_6 concentration.[28]

PLIF images are acquired using two separate Apogee charge-coupled device (CCD) cameras to gain optical access to both early time and later time flow structures. A 2184 × 1470 CCD array Apogee 32ME with 3 × 3 on-chip binning was used to acquire early times, including the ICs. The binning was performed to increase signal intensity and results in a 728 × 490 image. This camera is labeled "IC" in Figure 1, and is tilted with respect to the measurement plane to gain optical access to the initial conditions. Later times were acquired with an Apogee Alta U-42 camera with a 1024 × 1024 CCD array, labeled "DYN" in Figure 1, aligned orthogonally to the measurement plane. Each camera is equipped with a Tamron SP Macro lens with a focal length of 90 mm, and a visible-light interference filter to prevent contamination of the fluorescence signal by the 532 nm light scattered off the glycol particles. Both PLIF cameras provide high resolution images with about 50.5 μm/pixel. With only two PLIF laser pulses available for a single run of the experiment, the pulses could be timed to acquire two dynamic images, or one dynamic image and one IC image.

C. *x-t* diagrams

Figure 4 shows x-t (position versus time) diagrams with shock waves, reflected shock waves, and expansion fans, for $M = 1.21$, 1.36, and 1.50 experiments. Each x-t diagram shows the location of the interface within the test section and the rise in each pressure transducer signal (squares) giving the general space-time of an experimental run. The pressure signals agree with the 1D calculation of the incident shock, but the reflected shock wave is slower than ideal due to losses that occur in the experiment because of openings in the test section for the initial conditions.

III. IMAGE PROCESSING

The raw PLIF images are 2D maps of fluorescence intensity that scale linearly with acetone concentration (volume fraction) in the power output range of the PLIF laser. PLIF images are
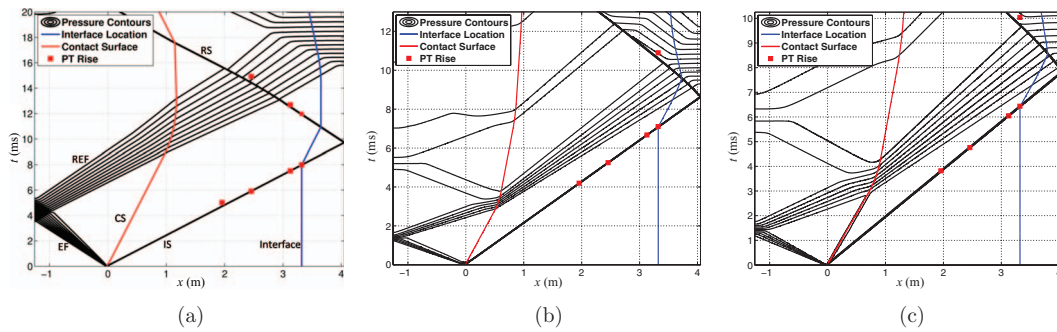
FIG. 4. Theoretical x(m)-t(ms) wave diagram for (a) Mach 1.21, (b) Mach 1.36, and (c) Mach 1.50 with experimental pressure trace rises overlaid (red squares). $x = 0$ is the location of the diaphragm. IS, incident shock; RS, reflected shock; EF, expansion fan; REF, reflected expansion fan; CS, contact surface; Interface, location of the gas curtain.

calibrated to concentration by first subtracting backgrounds to remove noise due to ambient light sources in the laboratory. Background images were taken approximately every 10 runs of the experiment, or whenever camera position was changed, by pulsing each laser head once in the absence of acetone.

The next correction was for variations in the uniformity of the laser sheet. Images of the laser sheet were obtained using a customized calibration test cell, shown in Figure 5(a), filled with the heavy gas mixture directly from the settling chamber. The cell is oriented so that laser light passes through the test cell via UV-transparent, fused silica windows 1 and 2. A spatial map of the light sheet is shown in Figure 5 for both laser heads at each camera position. As the light travels through the gas-filled test cell, the signal attenuates according to Beer's law.[29] This signal attenuation and the spanwise spread of the light sheet are corrected during processing. Because the fluid layer is thin and the acetone concentration at the measurement plane is small ($<15\%$ by volume), the Beer's law attenuation of the laser sheet across the mixing layer can be neglected in the current study.

Some small-scale laser sheet striations appear in corrected images due to small variations in laser performance, but they are relatively small in magnitude compared to pre-processed images. Figure 6 demonstrates the fidelity of the spanwise laser sheet correction in an IC image and a late time dynamic image. Figure 7 shows streamwise centerline profiles of the IC images (a) and (c) from Figure 6, as well as a line profile of the laser sheet image in Figure 5(b) at the same CCD location. Each of the profiles is normalized by the maximum value. The peaks in the intensity signal from the raw image follow the trend of the laser sheet variations in the spanwise direction (y). After correction, the calibrated image produces consistent peak values for each wavelength, all around a normalized value of one.
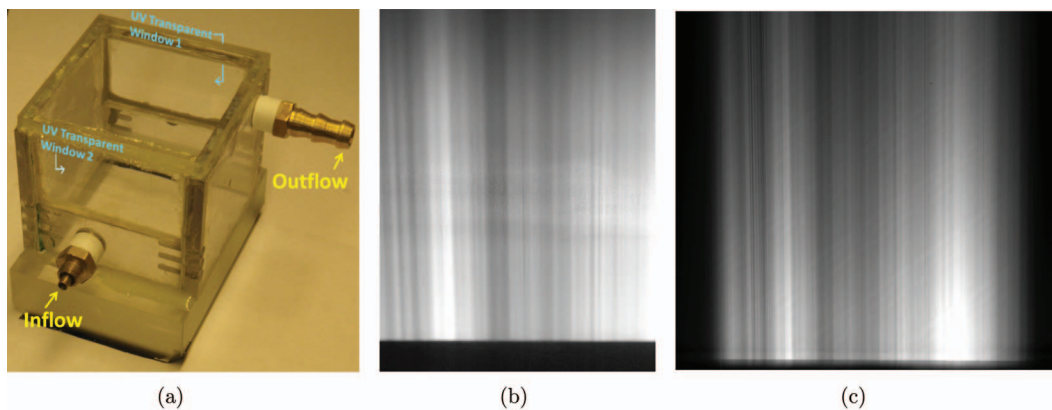

FIG. 5. (a) Photograph of test cell used for spanwise laser variation and volume fraction calibrations, and PLIF imaging of the laser sheet using the calibration test cell, with background subtracted for (b) IC and (c) DYN cameras.
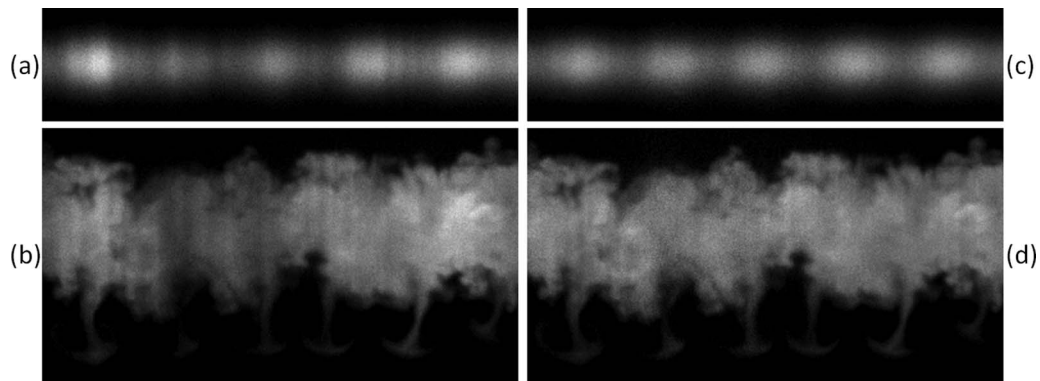
FIG. 6. PLIF images of Left: (a) ICs before laser sheet correction, and (b) a Mach 1.50 experiment at 1200 μs before laser sheet correction. Right: (c, d) The same images after correction.

Next, the images are converted from intensity to concentration. With infrared spectroscopy, the volume fractions of the gases in the settling chamber are known to be 75%/20%/5% for SF_6/acetone/air, respectively. All IC camera images are corrected for perspective error (arising from the nonorthogonal alignment of the IC camera to the imaging plane) by using a second-order polynomial transform to map the distorted image onto an orthogonal grid.

Because it was not possible to achieve post-shock conditions in the calibration test cell, post-shock images could not be calibrated directly. Instead, this was accomplished by equating the sum of the intensity field in each image with that of a calibrated and transformed reference IC image, following the principle of conservation of mass. This step accounts for differences in fluorescence due to post-shock temperature increases, differences in the response of the two cameras, and differences in laser intensity from pulse to pulse (known to be $\pm3\%$) without requiring the relevant calibration data. This method relies upon several assumptions including that the laser light sheet thickness is roughly constant with streamwise position, the mass of the heavy gas within the imaging plane of the ICs is the same for each run of the experiment, and that the net flow of mass across the boundary of the measurement region after shock interaction is negligible within a given experiment. The
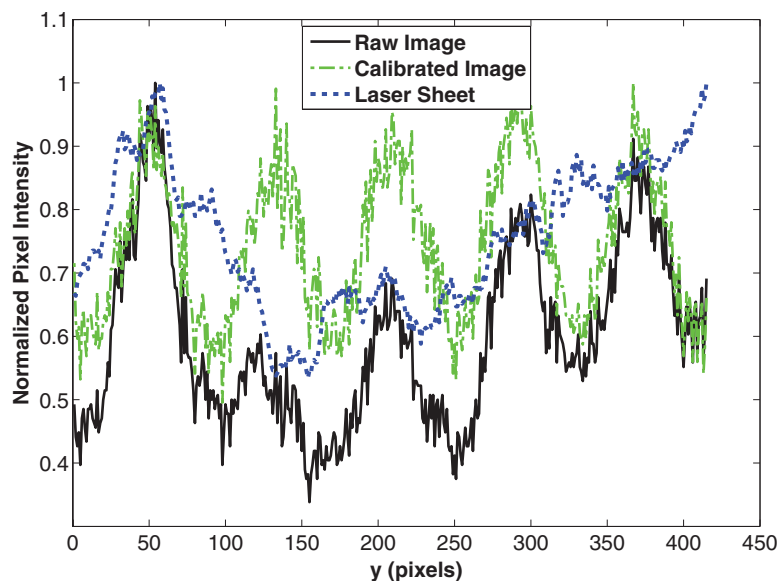

FIG. 7. Normalized intensity profiles along the center line of the IC image before (Figure 6(a)) and after spanwise correction (Figure 6(c)), and a line profile of the laser sheet shown in Figure 5(b) at the same pixel location.
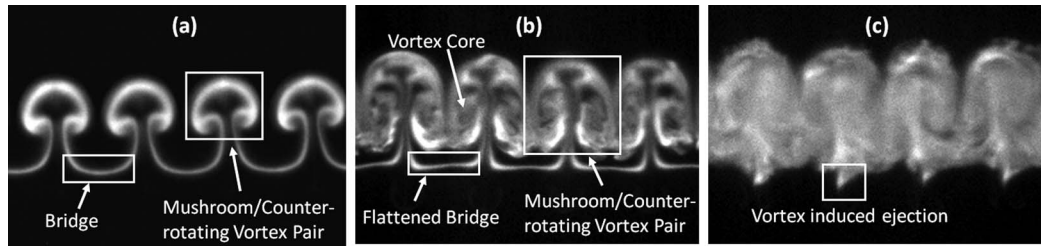
FIG. 8. Sample density maps from Mach 1.50 experiments indicating flow field nomenclature used in the body of the text. Images were acquired at (a) 125, (b) 300, and (c) 475 μs.

resulting images, with intensity proportional to the acetone concentration, can then be converted to SF_6 volume fraction, mass fraction, or density, ρ, using 1D gas dynamics.

IV. RESULTS

We use several density-field quantities to describe mixing in terms of extent, uniformity, and thoroughness, and to compare the evolution of the mixing layer for the three Mach number cases. Figure 8 gives a visual description of the flow feature nomenclature used in this report, while a list of parameters that govern the flow can be found in Table I.

As was discussed in Sec. II, only two PLIF laser pulses are available for each run of the experiment, so time series are acquired using multiple runs of the experiment. A total of 507 individual PLIF images met qualitative and quantitative criteria (i.e., structure symmetry, structure shape, shock speed within $\pm 1\%$) for inclusion in the data analysis.

A. PLIF image time evolution

Figures 9–11 show time sequences of the evolution the heavy gas curtain for Mach numbers $M = 1.21$, 1.36, and 1.50. The images are SF_6 volume fraction maps with a contrast of 1% to 30% SF_6 volume fraction for all images. The images are labeled with time after shock interaction (μs) and distance traveled from the initial condition location (cm). Figure 12 demonstrates the time series image selection process by showing the repeatability of the Mach 1.50 experiments at 3 different post-shock times.

The images in Figures 9–11 show the initial conditions at $t = 0$ μs just before shock interaction with the upstream interface, the passage of the shock wave through the gas curtain, maximum compression after shock interaction, and the subsequent evolution of the instability. Perturbations on the upstream interface begin to grow immediately after shock interaction, while a phase inversion first takes place on the downstream interface. As the perturbations on both sides grow, they begin to interact, leading to mushroom-like flow patterns that are characteristic of the RMI. In time,

TABLE I. List of parameters governing the flow, with ′ denoting post-shock conditions when ambiguous.

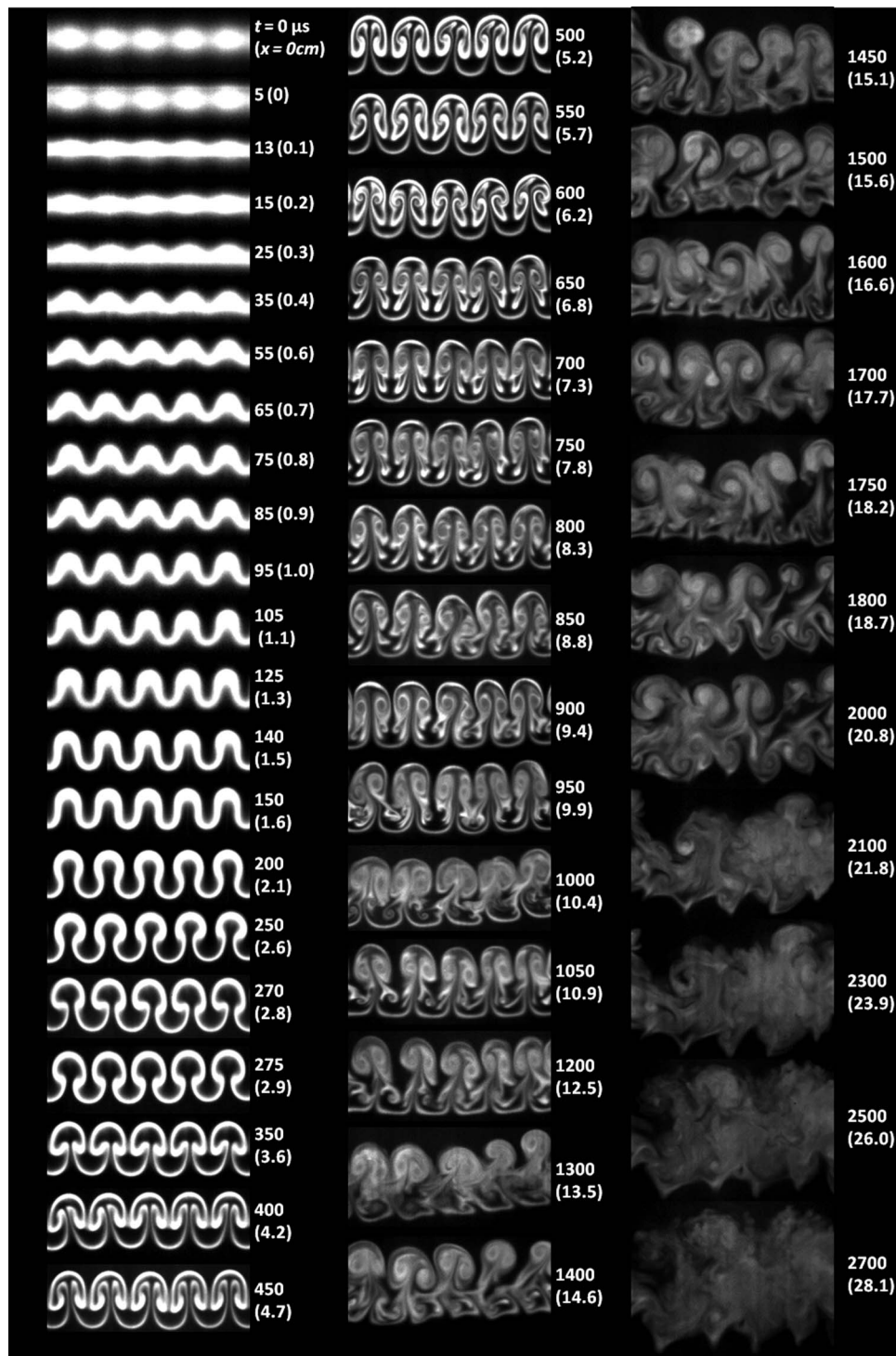|		Mach 1.21	Mach 1.36	Mach 1.50
Δv	(m/s)	104	158	222
δ_0	(mm)	3.8	3.8	3.8
δ_0'	(mm)	2.63	2.32	2.17
$\dot{\delta}_0$	(mm/μs)	0.013	0.029	0.042
κ	(mm^{-1})	1.744	1.744	1.744
Γ	(mm^2/μs)	0.07	0.09	0.13
A		0.49	0.49	0.49
A'		0.51	0.52	0.53
ν	(m^2/s)	1.1×10^{-5}	1.1×10^{-5}	1.1×10^{-5}
ν'	(m^2/s)	8×10^{-6}	7×10^{-6}	6×10^{-6}
$Re_{\Gamma, max}$		8×10^3	13×10^3	20×10^3

FIG. 9. Full time evolution of SF$_6$ volume fraction maps for Mach 1.21 experiments. Each image is labeled with time t and distance traveled (x). Contrast for all images is set at 1% to 30% SF$_6$ by volume fraction.

adjacent vortices begin to interact, causing an increase in the flow complexity within the mixing layer. Eventually, the flow transitions to smaller scale advective motions.

For ease of comparison between the different Mach number experiments, a subset of representative images from the complete time series in Figures 9–11 is shown in Figure 13. Images were
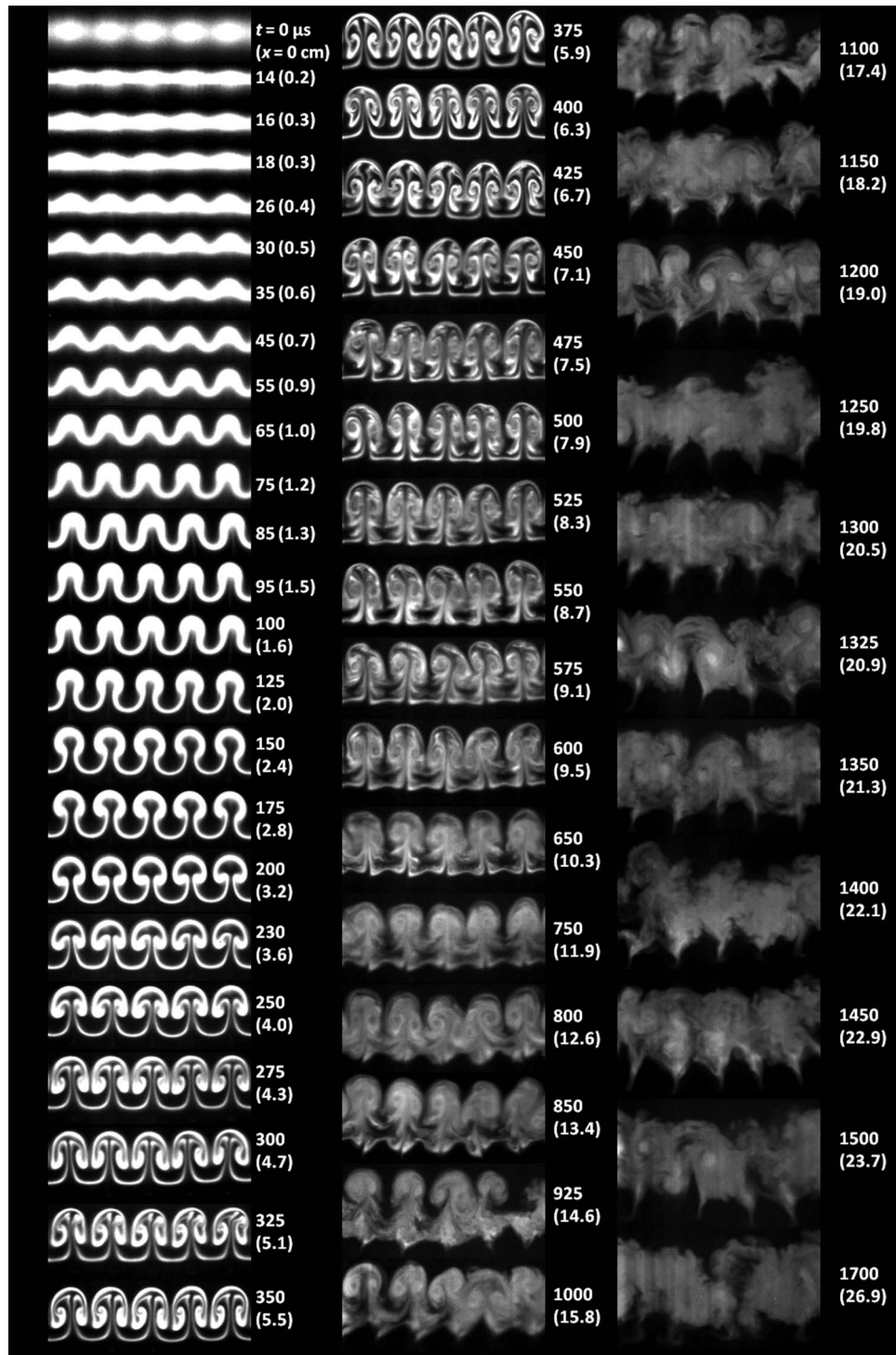
FIG. 10. Full time evolution of SF$_6$ volume fraction maps for Mach 1.36 experiments. Each image is labeled with time t and distance traveled (x). Contrast for all images is set at 1% to 30% SF$_6$ by volume fraction.

chosen to highlight the development of the instability throughout time, and images along a row are a similar distance from the IC location for each Mach number.

At early times, up to $x \approx 6$ cm, Figure 13 shows that the evolution for each Mach number is qualitatively very similar. The main difference at these times is due to the increased compression of
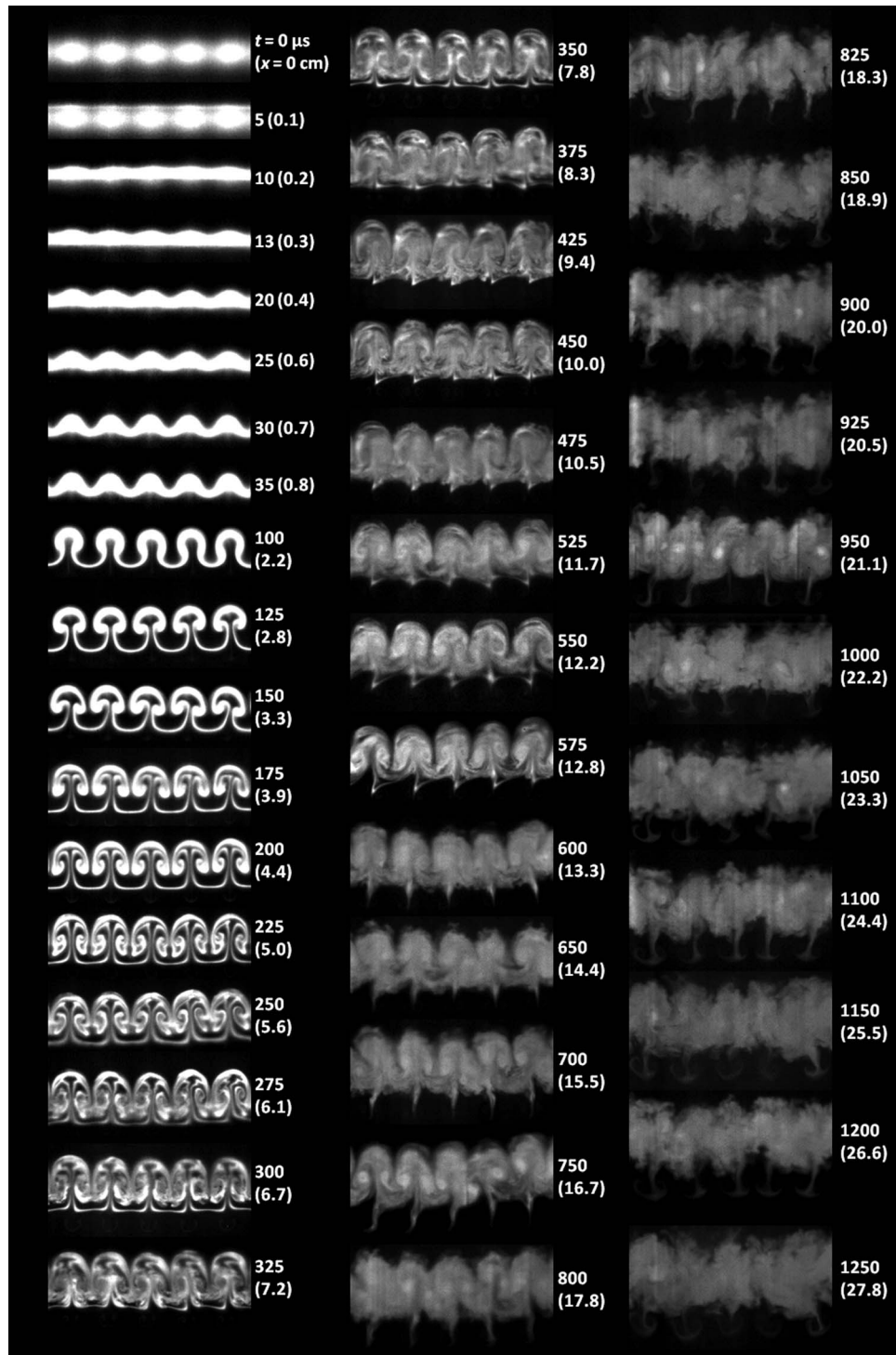
FIG. 11. Full time evolution of SF_6 volume fraction maps for Mach 1.50 experiments. Each image is labeled with time t and distance traveled (x). Contrast for all images is set at 1% to 30% SF_6 by volume fraction.

the curtain with higher Mach numbers. Another difference is that the bridges connecting mushrooms become increasingly flatter with higher Mach number (e.g., see $x \approx 4.5$ cm). Flattening of flow features with increasing Mach number has been observed in previous curtain experiments,[14] and single interface experiments,[13] and may be attributed to the proximity of the shock wave to the moving interface at higher Mach numbers.
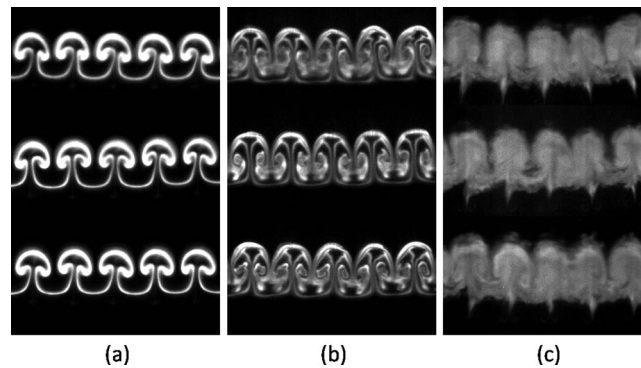
FIG. 12. Illustration of repeatability for the Mach 1.50 experiments: PLIF images from separate runs of the experiment at (a) 150 μs, (b) 275 μs, and (c) 600 μs after shock impact.

At intermediate times, from 6 cm to 13 cm, the structures begin to grow differently. More vorticity is deposited in the curtain by the higher Mach numbers, and more SF_6 is entrained by these stronger vortices. In Mach 1.21 experiments, the primary vortices are not strong enough to continue entraining all the SF_6 and tend to lag behind the center of the mixing layer. The primary vortices in the Mach 1.50 experiments dominate most of the mixing layer and remain located near its center. As the structures continue to roll up, this leads to differences in the structure development. By $x \approx 12$ cm in Figure 13, the weaker primary vortices in Mach 1.21 experiments have begun to pinch off the rest of the mixing layer, giving rise to a more elongated mushroom stem. In Mach 1.50 experiments, the stronger primary vortices pull the bridge material toward the spanwise center of each counter-rotating vortex pair, causing it to eject out ahead of the structure. This flow feature is labeled "vortex induced ejection" in Figure 8. Both mechanisms are observed in Mach 1.36 experiments, with primary vortex pairs lagging behind the streamwise center (leading to elongation of the mushroom stems), but the effects are slower when compared to the Mach 1.50 case.

At late times, $x > 13$ cm, the differences observed at intermediate times become enhanced. For Mach 1.21, the mushroom stems continue to elongate, whereas for Mach 1.50, rapid growth of the vortex induced ejections is observed. For Mach 1.36, both mechanisms are observed. As time progresses, the ejected fluid in the higher Mach number cases rolls up into opposite facing mushrooms. For Mach 1.21, it is not until the latest times (after $x \sim 19$ cm) that what was formerly bridge material, begins to protrude out from the mixing layer, leading to a jagged interface on the downstream side.

There is a higher degree of uniformity across the mixing layer with higher Mach number. For Mach 1.50, the stronger vortices stir the entire width of the mixing layer, except for the ejected material, leading to a slightly earlier transition to smaller scale advective motions that tend to homogenize the concentration field throughout the layer. For example, compare the uniformity of mixing at $x \sim 19$ cm in Figure 13. Another effect of the stronger vortices is that they help to preserve spanwise symmetry with angular momentum as the mixing layer develops in time. For Mach 1.21 experiments, small differences in vortex strength between two counter-rotating vortices cause the mushrooms to tilt to one side or another, and sometimes to grow into an adjacent mushroom, disturbing its evolution. As Mach number is increased, spanwise symmetry is maintained longer.

B. Vorticity maps and circulation

The time evolution of the 2D vorticity fields (curl of the velocity field, $\vec{\omega}_z = \partial \vec{v}/\partial x - \partial \vec{u}/\partial y$), measured simultaneously with the concentrations fields, is shown in Figure 14, with color scale held constant for all maps. The numbers in parentheses represent the streamwise position of the structures in centimeters, with images along a row acquired at roughly the same scaled time, x. As expected, values for vorticity are higher in the higher Mach number case, where the primary vortices also dominate a greater region of the flow. These differences account for the disparity in
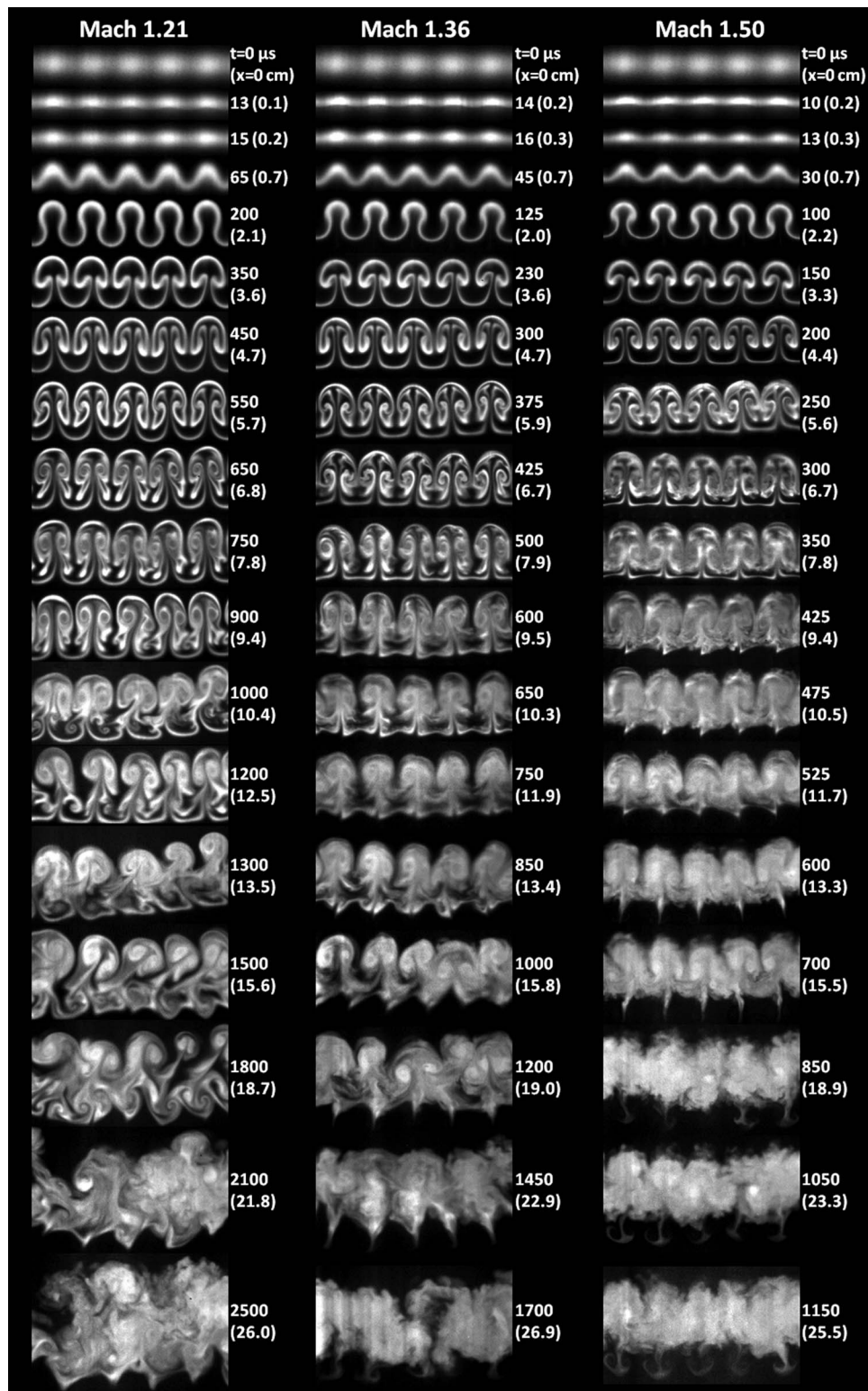
FIG. 13. A selection of SF_6 volume fraction maps from each Mach number experiment, with contrast customized for each image. Images in each row were acquired at roughly the same location as indicated in the figure, with time t and distance traveled (x).
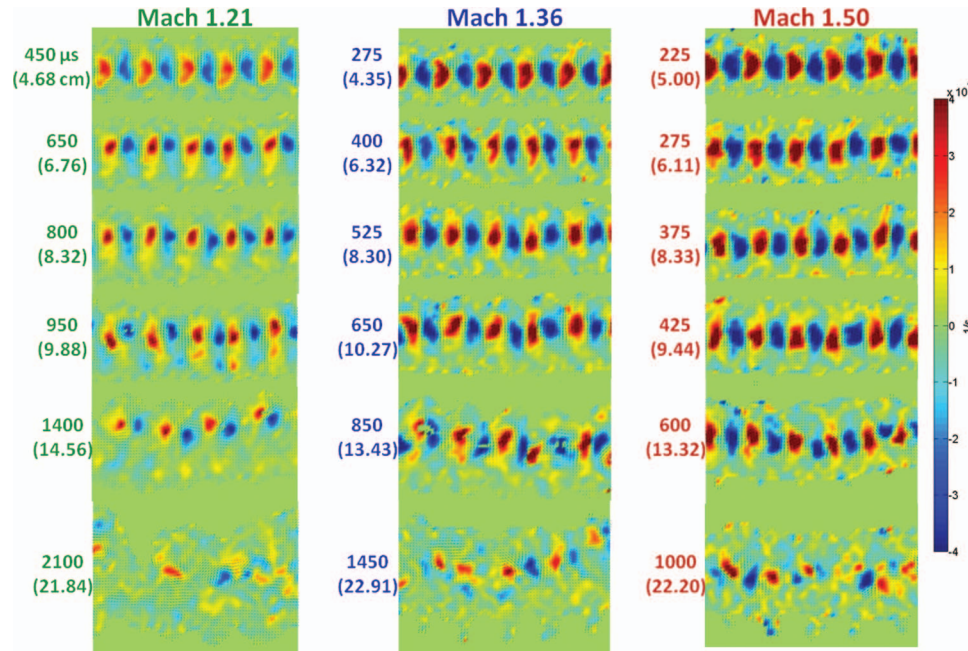
FIG. 14. Mach number comparison of vorticity map evolution shows the breaking down of the primary vortices over time.

large scale flow morphology seen in PLIF images at later times, as discussed above. In each case, as time progresses, the array of alternating blobs of positive and negative vorticity begin to lose their symmetry, precipitating a transition of the vorticity field to a more disordered state and a breaking down of the primary vortices into smaller vortices.

Circulation, Γ, was calculated from the velocity field via a line integral of the tangential velocity component, $\Gamma = \oint \vec{u} \cdot d\vec{l}$ by enclosing a positive vortex within a rectangular path. For each velocity field, up to 5 vortices were chosen, and the circulation of each was used to get an average value for circulation in a given field. Figure 15(a) shows an example of the rectangular regions used to calculate average circulation for a single velocity/vorticity map. Figure 15(b) shows the average circulation
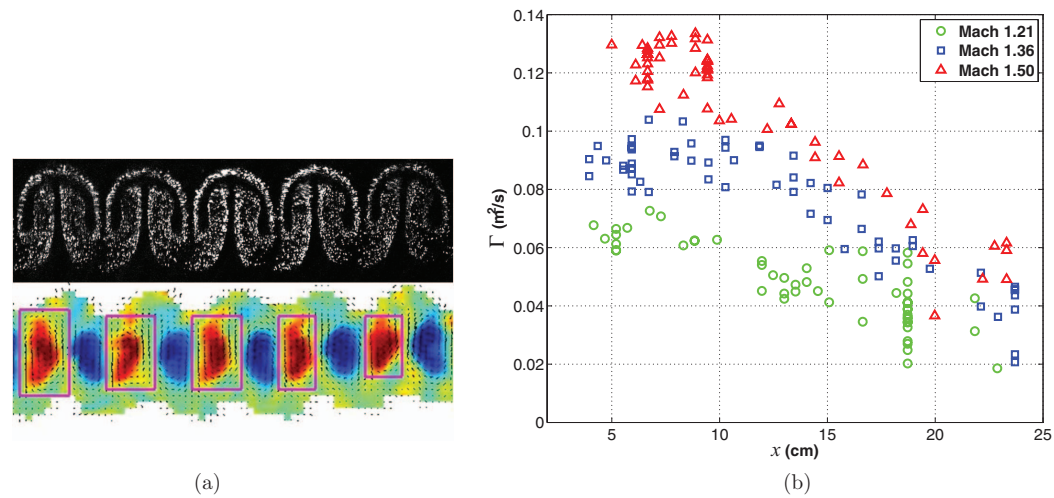

(a)

(b)

FIG. 15. (a) Up to five wavelengths were used to calculate an average circulation of positive vortices for each time. The top image shows the raw PIV data at 300 μs in a Mach 1.36 experiment, for an example. The bottom image shows the velocity field with arrows, and vorticity with the color map. The magenta boxes indicate the path along which the line integral was calculated. (b) Mean circulation as a function of distance traveled, x.

of the main vortices with distance traveled for each Mach number. The decrease in circulation over time provides evidence that energy is being transferred from the primary vortex pairs to smaller scales in the flow. It is also possible that some energy is being transferred into the third component out of plane. Between $x = 6$ and 10 cm, when the primary vortex cores have formed, but before they begin breaking down to smaller scales, the average values for Γ are approximately 0.07, 0.09, and 0.13 mm^2/μs for $M = 1.21$, 1.36, and 1.50, respectively.

A circulation based Reynolds number can be defined as

$$Re_\Gamma = \frac{\Gamma}{\nu}, \tag{3}$$

where ν is the kinematic viscosity. To estimate a single post-shock value of kinematic viscosity (ν'), post-shock conditions, and the average mixture composition across the initial conditions were used to estimate a single post-shock value of dynamic viscosity (μ') for each Mach number following the method of Reid *et al.*[30] The maximum measured Re_Γ occurs between $x = 5$ and 10 cm for each Mach number and is approximately 8 000, 13 000, and 20 000 for Mach 1.21, 1.36, and 1.50, respectively. This measure of Reynolds number is limited to early and intermediate times, before the primary vortices break down. At later times, a Reynolds number based on turbulent kinetic energy is more appropriate.

C. Mixing layer width

The total width of the mixing layer is a common quantitative metric to quantify large scale flow dynamics and is widely used in the study of R-M flows to compare between different experiments, models, and simulations. We define mixing layer width (δ) as the distance spanning the farthest upstream and downstream locations at which 5% SF$_6$ by volume fraction ($c_v = 0.05$) is present, measured over one perturbation wavelength at the same spanwise location for each time, as shown in Figure 16.

In Figure 17(a), δ is shown versus time for all of the time series images from Figures 9–11. Error in width measurements reported here is estimated to be within ±5%. At late times, the flow features discussed above cause a secondary jump in the growth rate for each Mach number. For Mach 1.21, it is mainly due to the lag of the main vortices, whereas for Mach 1.50 it is due to the ejections ahead of the downstream interface that are formed by the interaction between the relatively stronger main vortex pairs. For Mach 1.36, both secondary growth rate mechanisms (lag and ejections) contribute.

Previous R-M studies have shown that mixing layer width can be effectively scaled amongst experiments at different Mach numbers, both for single interface and double interface gas curtain experiments. Most experimental efforts to scale growth rate have been motivated by
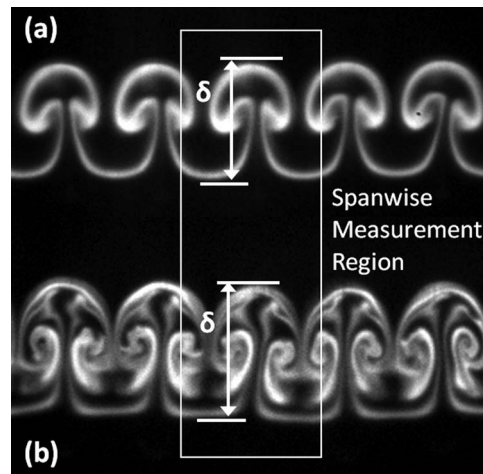

FIG. 16. Definition of mixing layer width, δ, using Mach 1.35 experiments at (a) 230 μs, and (b) 425 μs. The width is the distance between the farthest upstream and downstream extents at which at least 5% SF$_6$ volume fraction is present.
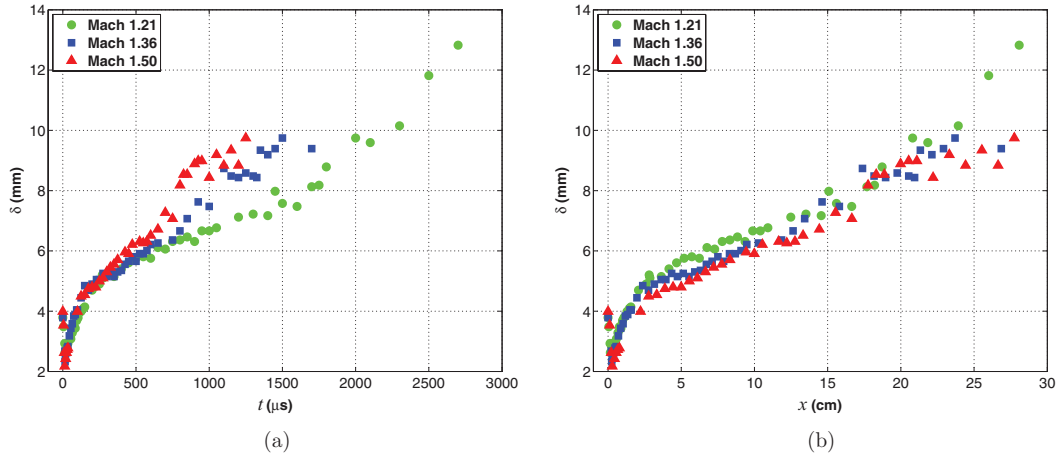
FIG. 17. (a) Mixing layer width vs time. (b) Mixing layer width vs distance traveled shows the same growth rate for each M, but with a vertical offset separating the experiments until $x \approx 15$.

nondimensionalizing Richtmyer's linear formulation so that

$$\kappa a - \kappa a_0 = \kappa^2 a_0 A \Delta v t. \tag{4}$$

The nondimensional time is then taken as

$$t^* = \kappa^2 A \Delta v a_0 t, \tag{5}$$

and the nondimensional perturbation amplitude is then $\kappa a - \kappa a_0$, where it has sometimes been found that the fidelity of the scaling can be improved if the post-shock or the average of pre-shock and post-shock values of a_0, or A are used. In studies where the linear growth regime can be measured experimentally, the term $\kappa a_0 A \Delta v$ can be replaced by $\dot{a}_0$,[16,23] the measured initial growth rate, assuming that linear stability is a reasonable estimate for the growth, so that

$$t^{**} = \kappa \dot{a}_0 t. \tag{6}$$

This scaling has proven to be more effective than Eq. (5), presumably because it accounts for the finite diffusion thickness present in experiments that is not accounted for in Richtmyer's impulsive model, as well as any other effects due to the passing shock wave. This scaling cannot be used to predict growth rates because it requires that experiments must first be performed for each initial condition and each Mach number. When the initial growth rate cannot be experimentally measured, a growth rate reduction factor can be added to the impulsive model, and therefore to t^*, to improve the scaling by accounting for the reduction in growth rate when the interfacial density profile has some slope, as opposed to being discontinuous.[13,16]

The growth of mixing layer width, δ, is dependent upon the growth of the perturbations, da/dt on both sides of the fluid layer. In the limit of a thick curtain with no interaction between the two interfaces, one would expect $d\delta/dt = 2da/dt$ based on Richtmyer's formula, for small-amplitude initial perturbations. Previous gas curtain experiments introduced the nondimensional time parameter[14]

$$\tau = 2\kappa A \Delta v t. \tag{7}$$

Here τ does not include a dependence on a_0 because it is difficult to quantify due to the diffusion thickness in curtain experiments. Because t^{**} lacks predictive capability and simply forces a curve fit at early times, and because τ is not universal for a variety of initial conditions because it does not include a dependence on a_0, both methods of scaling the time axis are lacking. In the present study, the only parameter that changes with Mach number and affects the growth according to the linear stability formulation is Δv, if only pre-shock values are considered. Therefore, it is preferred in the current study to scale the time axis with the velocity jump (synonymous with convection velocity in the present experiment) of the mixing layer so that it is a function of distance traveled, x, so the parameters following will include comparisons between Mach number experiments at the
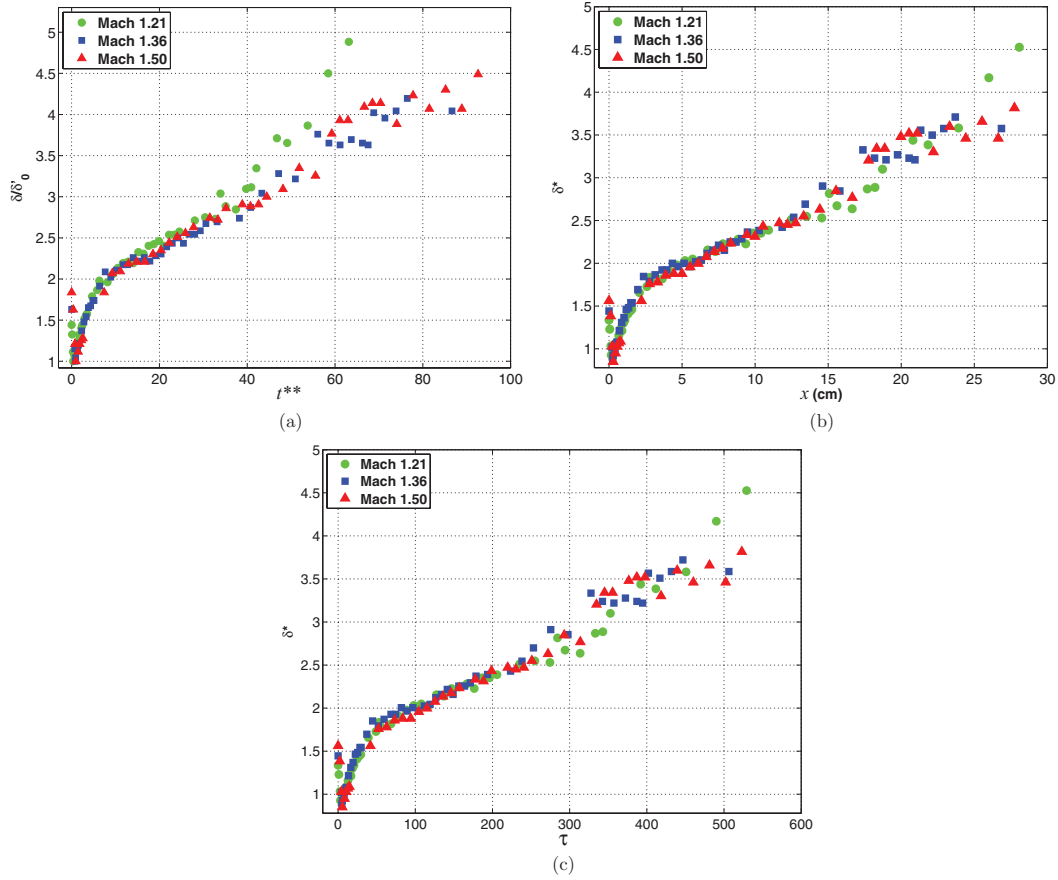
FIG. 18. (a) δ/δ_0' vs t^{**} collapses the data up to $t^{**} = 40$. (b) δ^* vs distance traveled collapses the data to $x \approx 25$. (c) δ^* vs τ collapses the data to $\tau \approx 475$.

same downstream location. While simple, this method of scaling the time axis appears remarkably effective for the current set of initial conditions within the considered Mach number range, as observed in Figure 17(b). But for comparison to the previous work available in the literature, plots with t^{**} (with $\dot{\delta}_0$ replacing $\dot{a}_0$ in Eq. (6)) and τ are also presented in Figure 18.

Plotting width against distance traveled, as in Figure 17(b), achieves an effective collapse of the data in the sense that the growth rate with distance traveled is equivalent for each Mach number case until the latest times where the Mach 1.21 structures grow faster. This tertiary growth rate increase for Mach 1.21 experiments occurs after 23.5 cm, and appears due to the interaction of bridge material that leads to the jaggedness observed on the downstream interface. The average convection velocity for the structures was measured using PIV data by ensemble averaging over the mean streamwise velocity for each mixing layer within a given Mach number experiment, so that $\langle \bar{u} \rangle = \Delta v = 104$, 158, and 222 m/s for $M = 1.21$, 1.36, and 1.50, respectively. Overbars denote averaging within a given realization, and angle brackets denote ensemble averaging over a set of realizations.

Normalized width (δ/δ_0') versus t^{**} is shown in Figure 18(a). Using the measured early time growth rate (calculated from $t^{**} \leq 4$) to scale the time axis forces a collapse of the data at these early times, however a fairly good collapse of the data is maintained well past $t^{**} = 4$ to $t^{**} \approx 40$ with the Mach 1.21 experiments growing faster thereafter.

The most effective way to collapse the growth rates for the longest duration of time is to plot x (or equivalently, τ) against a nondimensional width, δ^*, defined as

$$\delta^* = \frac{\delta}{\delta_0'} M^{-0.4}. \tag{8}$$

In Eq. (8), the width is scaled both by the initial post-shock width, and the Mach number, M, of the experiment. The δ^* scaling was first introduced by Anderson[31] to collapse single cylinder initial condition numerical experiments with Mach numbers ranging from $M = 1.2$ to $M = 2.5$, and was determined empirically. As seen in Figure 18(b), this scaling does a remarkable job of collapsing the present gas curtain experiments up to $x \approx 25$ cm ($\tau \approx 475$).

While mixing layer width is a useful metric to compare among experiments, simulations, and models, and is a simple measurement to make, it is very limited in what it says about mixing and the mechanisms that drive it, especially at smaller scales in the flow. For example, secondary growth is observed for each Mach number case at roughly the same scaled time, yet appears to occur as a result of different mechanisms for each case. These differences are not captured by the width measurement. Previous experiments have shown that quantitative measurements of smaller scale features, such as the instantaneous mixing rate, do not scale similarly with velocity.[14] This highlights the need for additional metrics to compare among experiments, simulations, and models, and to gain an understanding for the physics involved in the mixing process.

D. Mixing area and mean volume fraction: Measures of mixedness

Given a fixed amount of heavy gas, an increase in the area where heavy gas is present implies an increase in molecular mixing with pure air, and therefore provides a direct measurement of how much mixing has taken place. The total area over which there exists concentration at or above the 5% SF_6 volume fraction level is shown versus distance traveled in Figure 19(a). Total area gives a sense of how spread out the mixing layer has become in two dimensions, and is more useful for quantifying the degree of mixing than the total width, δ (presented above in Sec. IV C), because measurements of δ can be strongly influenced by projectile features that do not make large contributions to the molecular mixing of the two fluids. In fact, an increase in δ does not even necessarily imply an increase in the amount of mixing as we refer to it. Rather, it is a direct measurement of the bulk interpenetration of one species into the other, which in this experiment is dominated by advection.

As can be seen in Figure 19(a), after $x = 10$ cm, the total area decreases with increasing Mach number, implying the somewhat counterintuitive result that lower Mach number shock waves generate more mixing of the SF_6 with the surrounding air over a given distance traveled. A related measure of mixedness is the mean volume fraction of SF_6 among all pixels that contain signal, $\overline{c_v}$. Only those pixels at or above the 5% SF_6 volume fraction level were considered. Shown in Figure 19(b) is $\overline{c_v}$ versus distance traveled. Because the PLIF images were processed using a conservation of mass assumption, an increase in area always results in a corresponding decrease in $\overline{c_v}$. Therefore, after 10 cm, $\overline{c_v}$ is smaller for lower Mach numbers, also implying more mixing for lower Mach numbers over a given amount of distance traveled.
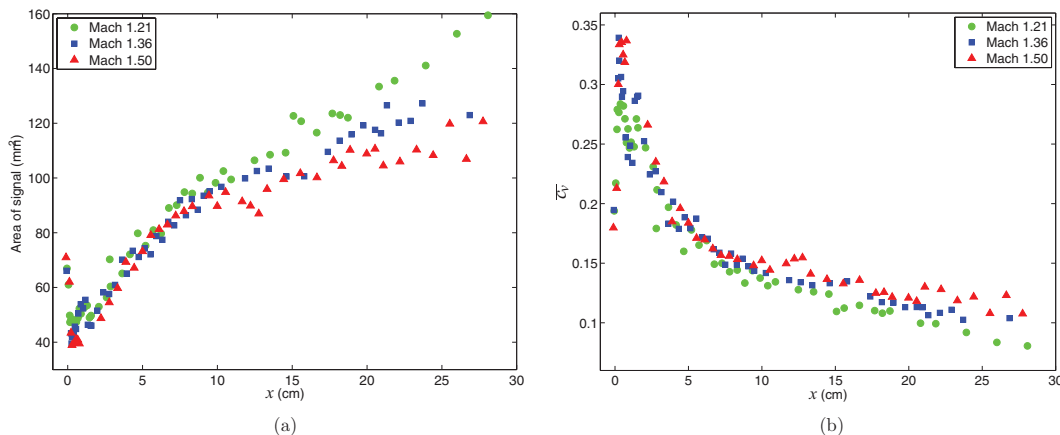

FIG. 19. Measures of mixedness: (a) area of PLIF signal as a function of distance traveled, and (b) $\overline{c_v}$ as a function of distance traveled.
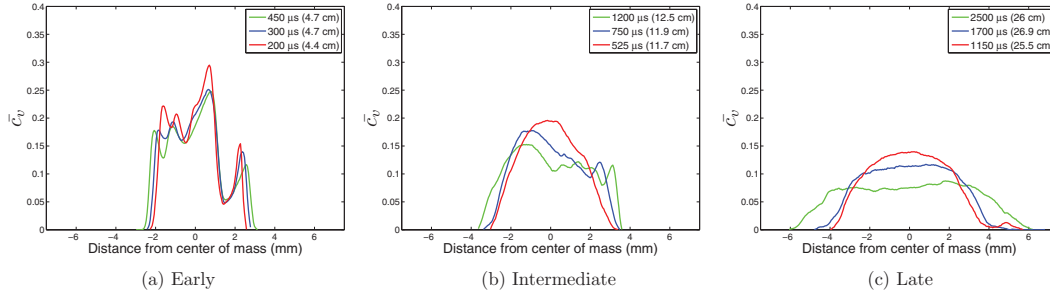
FIG. 20. Streamwise profiles of mean volume fraction of SF$_6$, $\overline{c_v}(x)$. Plots compare $\overline{c_v}(x)$ for each Mach number for 3 different scaled time regimes.

E. Streamwise profiles of mean volume fraction and volume fraction PDFs

While the total signal area and $\overline{c_v}$ indicate how much air has mixed with SF$_6$, the streamwise profile of the mean volume fraction of SF$_6$, $\overline{c_v}(x)$, can indicate how uniform the mixing is. Figure 20 compares $\overline{c_v}(x)$ for each Mach number at nine different scaled times, with the center of mass location indicated by 0 mm on each horizontal axis. It is important to note the distinction between $\overline{c_v}$, the mean volume fraction of SF$_6$ among only those pixels that contain signal, and $\overline{c_v}(x)$, the mean volume fraction of all pixels along a given streamwise location. The plots of $\overline{c_v}(x)$ in Figure 20 are similar for each Mach number in terms of the number of local peaks and troughs until intermediate times beginning at 6 cm scaled time, when the structures begin to grow differently (as it was noted in Sec. IV A). The existence of multiple peaks and troughs illustrates a lack of uniformity of the mixing across the mixing layer. Conversely, a top hat shaped profile would indicate completely uniform mixing, in a spanwise averaged sense. By ∼7 cm (not shown in Figure 20), the number of local peaks in the Mach 1.50 experiments decreases. At this scaled time, the number of local peaks in $\overline{c_v}(x)$ is 5, 4, and 3 for $M = 1.21$, 1.36, and 1.50, respectively. By ∼16 cm (not shown in Figure 20) it is 3, 2, and 1 for $M = 1.21$, 1.36, and 1.50, respectively, indicating that mixing is indeed occurring more uniformly throughout the mixing layer, even in scaled time, as Mach number is increased. The Mach 1.50 case has the highest values of $\overline{c_v}(x)$, an indication of less overall mixing that is consistent with the observation from Figure 19(b).

Information about the amount and uniformity of mixing is also contained in probability density functions (PDFs) of the volume fraction of SF$_6$, shown in Figure 21. In the present flow, material projectiles that occur on the edges of the mixing layer can bias PDFs of the concentration field by including large regions of pure air if the PDFs are calculated over the entire mixing width, δ. Therefore, to measure the state of mixing near the core of the mixing layer where turbulent mixing is expected to be strongest, and to compare the effectiveness of the vortices from different Mach number experiments to generate mixing, the PDFs were calculated using the middle 20% (0.2δ) of the mixing layer. This region is centered in the x direction on the streamwise center of mass and
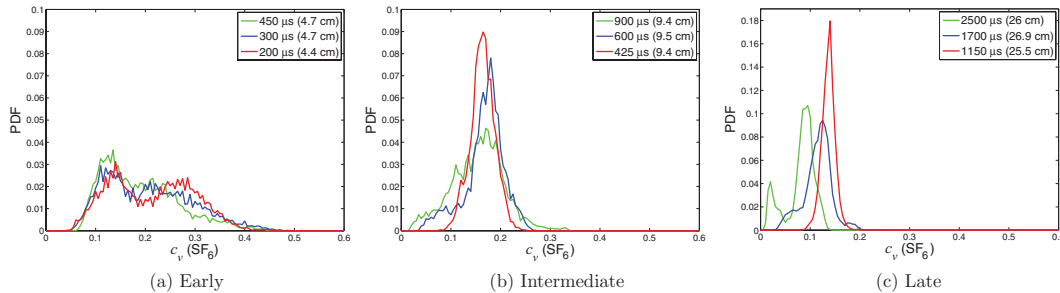

FIG. 21. PDFs for volume fraction of SF$_6$ for each Mach number at 3 different scaled time regimes.

spans all 5 wavelengths in the y direction. All pixels within the region were included in the PDFs, and bin size was set to $c_v = 0.005$ for all cases.

Figure 21(a) shows that at early times the PDFs have wide distributions and similar profiles for each Mach number. An obvious peak in the volume fraction PDFs first forms in the Mach 1.50 experiments after $x \sim 6$ cm. As time progresses, the peak distribution for all Mach numbers becomes increasingly narrow, indicating increasing mixing uniformity for all cases, with peak probabilities at higher concentrations for higher Mach numbers, indicating that as M increases less pure air is molecularly mixed with the heavy gas. A double peak is observed in some of the PDFs for Mach 1.21 experiments at later times (see Figure 21(c)). This structure reflects the large amount of low density gas that penetrates well into the mixing layer in low Mach number experiments. In Mach 1.50 experiments, the uniformity of the mixing layer is much higher, and this is quantified by the much narrower peak in the PDFs at $0.1 \leq c_v \leq 0.2$. In Mach 1.36 experiments there is no prominent second peak like in the Mach 1.21 case, but the distribution is not as narrow as observed in Mach 1.50 experiments.

F. Mixing progress variables indicating mixing uniformity

The density-specific-volume correlation, b, appears as an unclosed multiplier in the production term of the mass flux equation for variable density flows and is important for governing mass transport and fluid mixing in the current experiment.[32] We measure b in our experiments to understand the uniformity of mixing at the smallest scales of an instantaneous flow field.

The density-specific-volume correlation can be defined using fluctuating or mean density fields as[32]

$$b = \overline{-\rho'\left(\frac{1}{\rho}\right)'} = \bar{\rho}\,\overline{\left(\frac{1}{\rho}\right)} - 1. \tag{9}$$

By definition, b is non-negative and is equal to 0 when two fluids are homogeneously mixed. Conversely, high values of b indicate that the fluid is spatially inhomogeneous. In our curtain geometry, material projectiles that occur on the edges of the mixing layer can make large contributions to fluctuating quantities, biasing b to higher values. Therefore, for similar motivations discussed above for the method of calculating the concentration PDFs, the same middle 20% region was considered for calculations of b. Over this region,

$$b = \overline{\rho(x, y)}\,\overline{\left(\frac{1}{\rho}\right)(x, y)} - 1, \tag{10}$$

where spatial averages have been taken over both x and y. Averaging b over all realizations at each time then gives $\langle b \rangle$. The evolution of $\langle b \rangle$ is presented in Figures 22(a) and 22(b).
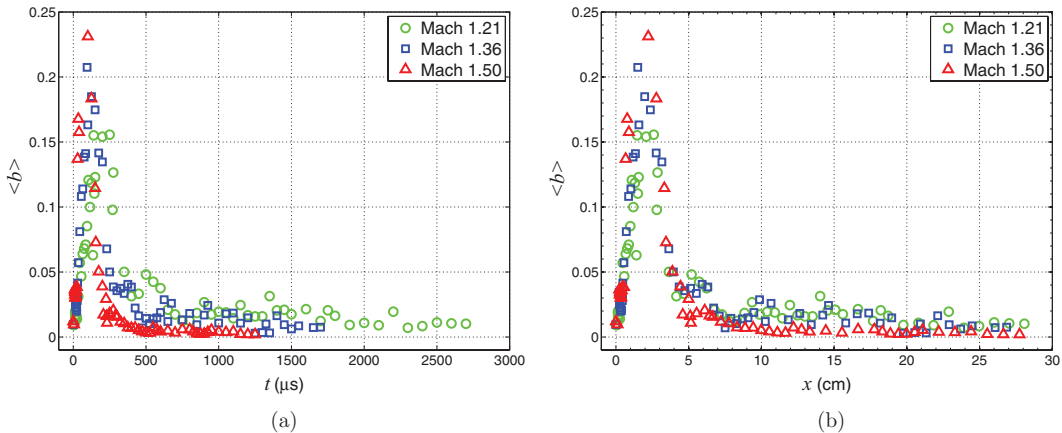

FIG. 22. (a) $\langle b \rangle$ as a function of time. (b) $\langle b \rangle$ as a function of distance traveled.

The value of $\langle b \rangle$ is initially low because the middle 20% of the layer contains only heavy gas. After shock interaction, the perturbations on the interface grow, and a peak in $\langle b \rangle$ occurs before the vortex cores are formed. Inspecting the images at $x \approx 2$ in Figure 13, one can see that the mixing layer is characterized by alternating regions of high density gas and pure air in the spanwise direction, and therefore $\langle b \rangle$ is relatively high. As the vortex cores cause the mixing layer to roll up, $\langle b \rangle$ decays until smaller scale mixing is observed in the cores. Thereafter, $\langle b \rangle$ does not change much and asymptotic behavior is observed. There appears to be a plateau in Figure 22(b) in the region of $4.5 \leq x \leq 6.5$ for each Mach number. It is during this time that the onset of small scale mixing in the vortex cores is observed, so this plateau feature serves as a quantitative marker for this transition. This plateau is a direct consequence of performing multiple experiments at each time with small noise variations in initial conditions. This resulted in some experiments undergoing a slightly quicker transition to small scale mixing than others. The standard deviation among images at a given time was highest for those in the $4.5 \leq x \leq 6.5$ window, with experiments where small scale mixing is not observed serving to raise the value of $\langle b \rangle$ at that time. By $x = 7$ cm, small scale mixing is observed in all images. That this transition occurs at a similar scaled time, independent of Mach number, is a pattern that can be used to aid turbulence modeling.

By $x = 4.5$ cm, and throughout the rest of scaled time, the value of $\langle b \rangle$ is lower for Mach 1.50 experiments, indicating greater homogeneity to the mixing layer as the stronger vortex cores are more efficient at stirring the available gas and thereby promoting reduction of concentration fluctuations, as observed in Sec. IV A. The slope of $\langle b \rangle$ after $x = 7$ cm is also negligible for Mach 1.5 experiments. The $\langle b \rangle$ data for Mach 1.21 and 1.36 experiments exhibit no significant differences over these scaled times ($x > 7$ cm), and on average are approximately 3 times greater than $\langle b \rangle$ for Mach 1.50 experiments. Linear fits to Mach 1.21 and 1.36 data after $x = 7$ have slightly negative slopes, indicating that mixing uniformity is still increasing over these times.

Another measure of mixing progress, Ξ, can be obtained through mixture composition fields, first applied by Cook and Dimotakis[33] to Rayleigh-Taylor flows. To calculate this mixing progress variable, concentration fields were first converted to normalized mole fraction, X, so that the X scale varies from 0 (pure air) to 1 (heavy gas mixture). The fields can then be transformed into mixture compositions, X_p, varying between $X_p = 1$ where a stoichiometric mixture of air and heavy gas is present, and $X_p = 0$ where there is only pure air or heavy gas,

$$X_p = \begin{cases} \frac{X}{X_s} & \text{for } X \leq X_s, \\ \frac{1-X}{1-X_s} & \text{for } X > X_s. \end{cases} \tag{11}$$

Here X_s represents the stoichiometric heavy gas mole fraction given the current state of the mixing layer, and was calculated for each image as the mean mole fraction of all pixels within the streamwise extents of the mixing layer. Using the nomenclature of Cook and Dimotakis,[33] Ξ is then the ratio of two differing mixing thicknesses,

$$\Xi = \frac{P_t}{P_m}, \tag{12}$$

where P_t is the total mixing thickness,

$$P_t = \int_{-\infty}^{\infty} \overline{X_p(X)}^y \, dx, \tag{13}$$

and P_m is the maximum possible mixing thickness,

$$P_m = \int_{-\infty}^{\infty} X_p(\overline{X}^y) \, dx. \tag{14}$$

For P_m the average mole fraction of each streamwise location (denoted by an overline with a y subscript to indicate spanwise averaging) is first obtained before transforming into a mixture composition field. Therefore, this measure of mixing thickness is always larger than P_t and describes the spatial extents over which there is interpenetration of the two gases, similar to δ, defined earlier. For this reason P_m is also referred to as "entrainment length."[18,34] Contrastingly, P_t represents a length related to where the two fluids have molecularly mixed. Ξ then indicates how much mixing
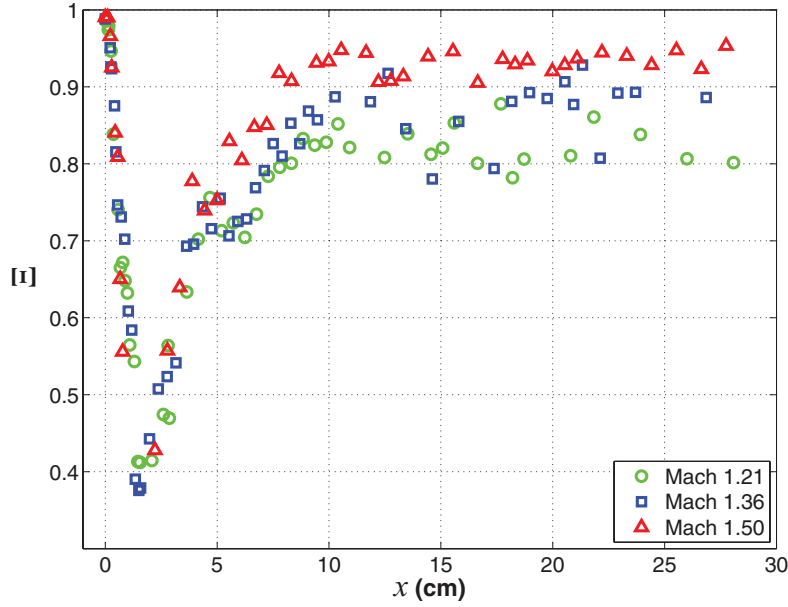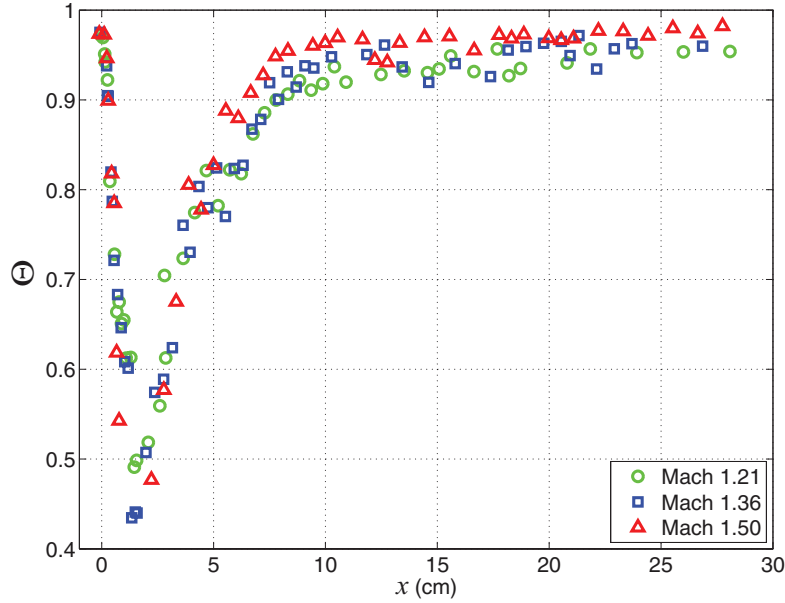
FIG. 23. Evolution of Ξ with distance traveled.

has occurred relative to how much mixing could occur if all entrained fluid were completely mixed at each streamwise location, and varies from 0 (if two fluids are spatially segregated) to 1 (if two fluids are uniformly mixed at each streamwise location).

In Figure 23, Ξ is shown versus distance traveled. Initially, Ξ is high for all cases, as the diffuse initial conditions are relatively uniform in the spanwise direction. As the deposited vorticity causes the instability to grow, air is entrained in the mixing layer, and thus Ξ decreases rapidly, reaching a low at $x \sim 2$ cm for each Mach number case. Small scale mixing mechanisms then begin contributing to mixing uniformity and Ξ begins increasing rapidly for each Mach number. After $x = 10$ cm, Ξ appears to asymptote for each case, with higher values reflecting the increased mixing homogeneity for higher Mach numbers. The average value of Ξ over the range $x \geq 10$ cm is 0.82, 0.87, and 0.93 for Mach 1.21, 1.36, and 1.50, respectively. A single interface RMI experimental study with a Mach 1.6 incident shock wave has reported Ξ = 0.85 at the latest measured time,[18] while numerical studies of the Rayleigh-Taylor instability[33,34] have reported late time values in the neighborhood of Ξ = 0.8.

The molecular mixing fraction, Θ, provides a similar measure of mixing homogeneity that has also been applied to Rayleigh-Taylor flows.[35,36] Θ is defined similarly to Ξ and has been found in numerical work to yield similar results,[34]

$$\Theta = \frac{\int \overline{f_1 f_2}^y \, \mathrm{d}x}{\int \overline{f_1}^y \, \overline{f_2}^y \, \mathrm{d}x},$$ (15)

where f_1 is the volume fraction of air, and $f_2 = 1 - f_1$ is the volume fraction of heavy gas. Again, the overlines with y subscripts represent averaging in the spanwise direction. Like Ξ, Θ varies from 0 if two fluids are completely segregated, to 1 if two fluids are uniformly mixed at each streamwise location. In Figure 24, Θ is shown versus distance traveled. Trends observed in the plots are similar to those of Ξ in Figure 23, although the differences in Θ between the Mach number cases at later times are less exaggerated. Average values of Θ in the $x \geq 10$ cm range are found to be 0.94, 0.95, and 0.97, for Mach 1.21, 1.36, and 1.50, respectively. These values are significantly higher than those reported in single interface numerical RMI experiments at 5 different Mach numbers,[37] where Θ ≈ 0.85 was found to be independent of Mach number.

FIG. 24. Evolution of Θ with distance traveled.

G. Instantaneous mixing rate

The availability of high resolution density maps makes it possible to investigate mixing at small length scales in the flow. The instantaneous dissipation rate of scalar fluctuations, $\chi(x, y, t)$ $\equiv D(\nabla c_v \cdot \nabla c_v)$, provides a measure of how quickly molecular mixing is occurring throughout the flow, and where it is occurring spatially. Therefore, it can be used to understand the processes that are driving the mixing between the two fluids, and what differences may exist between the different Mach number cases that leads to the results discussed in Secs. IV A–IV F. The molecular diffusivity between gases is estimated to be $D = 0.98 \times 10^{-5}$ m^2/s for air-SF$_6$. A detailed discussion of scalar dissipation in the context of turbulent shear flows is available in Ref. 38. This metric was first applied to RMI mixing by Tomkins *et al.*,[17] and has subsequently been used by other shock driven mixing investigations.[14, 18] The current study is the first to use quantitative concentration maps to calculate instantaneous mixing rates to study Mach number effects in RMI flows. Figure 25 shows spatial maps of $\chi(x, y)$, calculated using values for $c_v \geq 0.04$. The gradient at a given pixel location was calculated using the 8 adjacent pixels (4 orthogonal, 4 diagonal).

We calculated the total 2D diffusion-driven mixing rate, $\chi_{total} = \int\int \chi \, dxdy$, in each image by spatially integrating over the map of $\chi(x, y)$. Figure 26 shows χ_{total} versus time for each Mach number. At early times, as the deposited vorticity strains and stretches the heavy gas, the interfacial length is increased and the gradients are steepened, causing χ_{total} to increase rapidly, eventually reaching a peak where the diffusion based true molecular mixing is occurring approximately an order of magnitude faster ($\approx 15 \times$ as fast) than that of the curtain in absence of a shock wave. As the instability grows and small scale velocity fluctuations add to the straining and stirring, the structures become more mixed, resulting in less intense concentration gradients, and hence reduced instantaneous mixing rates. Because mixing occurs faster in real time for higher Mach numbers, χ_{total} falls off more rapidly with increasing Mach number after the peak value is obtained.

When we examine χ_{total} with distance traveled in Figure 27, we see that mixing rates are different and dependent upon Mach number. The higher Mach number experiments show a faster increase at early times and a slightly faster decrease after peak value, indicating a quicker transition to a more uniformly mixed state. This is confirmed with a qualitative inspection of the concentration maps in Figure 13 and the χ maps in Figure 25. In Figure 25, as the vortex cores roll up and their concentration gradients are reduced, their contributions to χ become increasingly smaller. While these active regions would be expected to contribute highly to the mixing rate throughout time, their
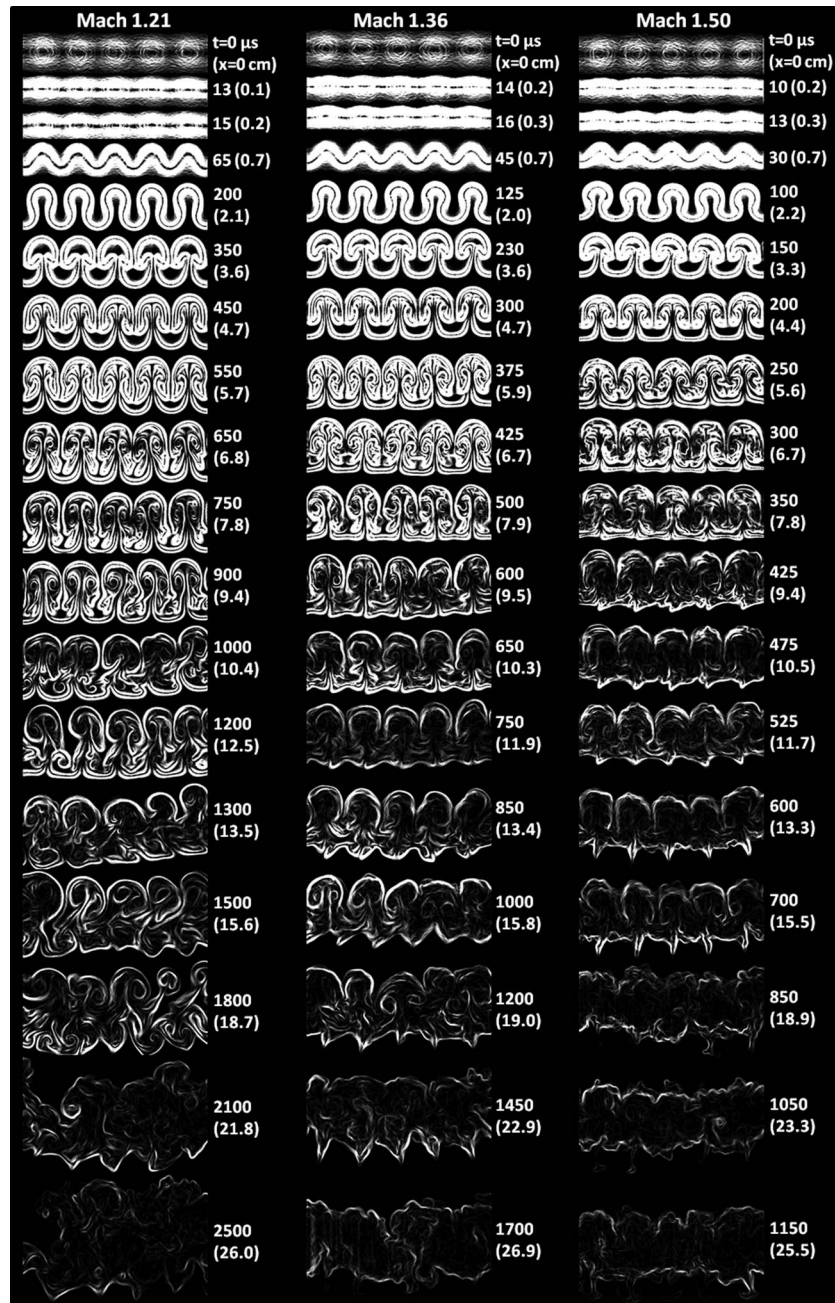
FIG. 25. Maps of $\chi(x, y)$ corresponding to the volume fraction maps in Figure 13, giving time, t, and distance traveled, x. Images are displayed on a log scale with intensity corresponding to $I = log(\chi + 1)$, and contrast set to $I = [0 : 0.3]$.

role may in fact be limited by the lack of freshly supplied air partly due to their location near the center of the mixing layer. This result was also observed by Tomkins et al.[17] Because the vortices are stronger in the higher M case, they stir a larger percentage of the mixing layer and crowd one another in the spanwise direction, effectively cutting off the available supply of pure air from penetrating into the mixing layer. Although the uniformity of mixing in these regions is relatively high, there is actually less pure air entrained into the mixing region for the higher M case compared to the lower M case.
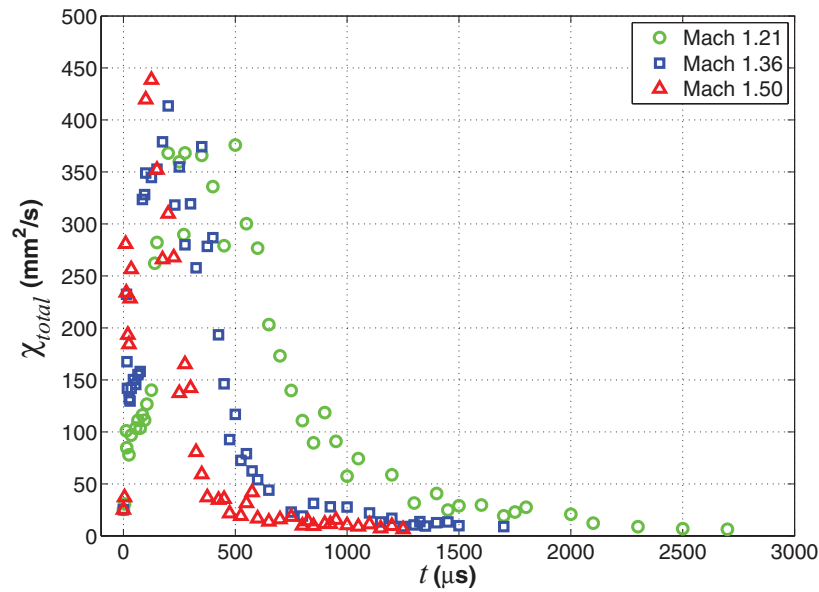
FIG. 26. χ_{total} as a function of time.

To quantify this observation, we look at the length of the interface defined at the $c_v = 0.05$ contour in Figure 28. The length of the $c_v = 0.05$ contour is important because it is indicative of the region over which molecular mixing occurs with pure air, providing information about the amount of mixing taking place with pure air, and the potential for more mixing with pure air to occur. The $c_v = 0.05$ contour was measured using an edge detection algorithm after masking the images in Figure 13. For most scaled times, the interface is longer with decreasing Mach number as a result of less compression of the initial conditions, and the differing vortex dynamics discussed in Sec. IV A. Although one may expect an increase in χ_{total} with increasing Mach number due to the greater amount of stretching and straining of the interface by the velocity field, and hence steeper
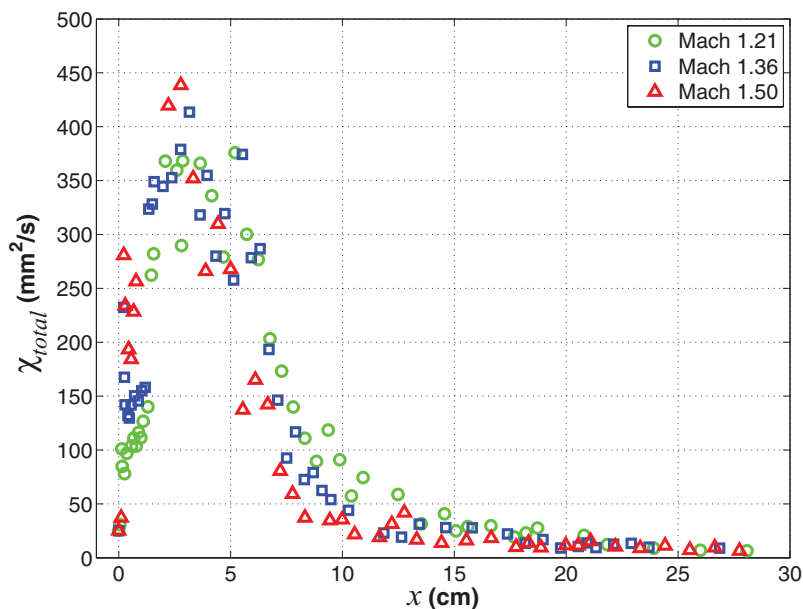
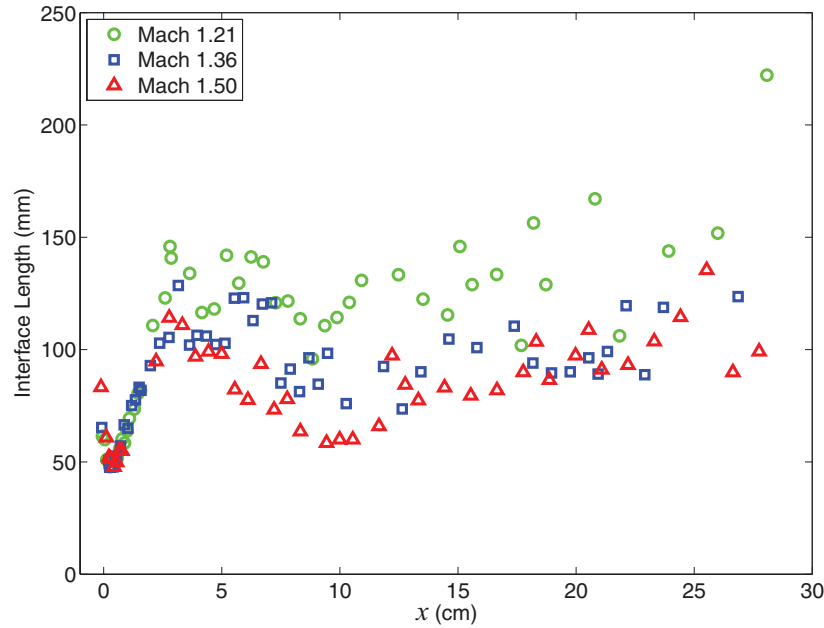FIG. 27. χ_{total} as a function of distance traveled.

FIG. 28. Interface length at the 5% SF_6 volume fraction level as a function of distance traveled.

gradients at early times, this effect is at least partially compensated for by longer interface lengths (where χ is the highest) in lower Mach numbers.

An indication of how much mixing has taken place can be obtained if χ_{total} is integrated over real time. It is apparent from Figure 26 that much higher values are obtained for lower Mach number if χ_{total} is integrated over time, and therefore, one can infer more molecular mixing for lower Mach number experiments.

The observation that lower Mach number shock waves generate more mixing at the same scaled time appears to be due to the additional absolute time and the additional interfacial length over which diffusion-driven molecular mixing acts. The interface length is a direct consequence of the dynamics of the vortex interaction, with stronger vortices limiting the amount of pure air that can penetrate into the mixing layer. Vorticity production is an important mechanism that determines the mixing state at later times by establishing the larger scale features. In addition to driving the energy transfer to smaller length scale advective stirring, the large scale features also drive the molecular mixing through diffusion. In higher Mach number experiments, the degree of advective stirring is higher, but this ultimately limits the amount of molecular mixing that can take place on average throughout the mixing layer.

V. CONCLUSIONS

We have found differences in both large- and small-scale mixing within a range of $1.2 < M < 1.5$ for fixed initial conditions by examining density and velocity fields in the temporally-evolving Richtmyer-Meshkov instability.

Scaling the time axis with the velocity jump (convection velocity in the present case) of the mixing layer is sufficient to collapse mixing width data. The remaining difference in width at the same scaled time appears to be the result of the curtain undergoing a greater amount of compression with increasing Mach number, and can be eliminated by scaling the width axis appropriately as well. The effectiveness of this scaling may not extend to higher Mach numbers where differences in post-shock Atwood number and compressibility effects may have a significant impact. The effectiveness of this scaling extends beyond the collapse of mix width growth rate data. For example, peaks in the evolution of b ($x = 2$ cm) and χ_{total} ($x = 3$ cm), the plateau feature in b (4.5 cm $\leq x \leq$ 6.5 cm), and

minima in Ξ ($x = 2$ cm) and Θ ($x = 2$ cm) occur at the same downstream location for each Mach number.

The quantities presented in this study provide information about how quickly mixing occurs, and how well mixed the two fluids become, both in terms of the uniformity of mixing throughout the layer, and the degree to which air and heavy gas molecularly mix. Even when compared at the same downstream location, measurements show that higher incident Mach numbers lead to a more uniform mixing state. Lower incident Mach number yields greater mixing at a given downstream location if 'mixing' refers to entrainment or interpenetration of one fluid into another (mixing layer width), or to the amount of originally unmixed fluid that undergoes some molecular mixing (determined directly by mixing layer area and mean volume fraction). Depending upon the specific application, the use of one definition over the other may be preferred for optimization.

These results are also explained via differing vortex dynamics measured in each Mach number case using PIV. In higher Mach numbers, the vortices are stronger, entrain more heavy gas, and grow larger. While more proficient at advective stirring and the reduction of concentration gradients that exist in their vicinity, the vortices in the higher Mach number experiments also serve to limit the amount of pure air available for continued molecular mixing throughout the layer. Therefore, the mixing layers in higher Mach number experiments are more uniformly mixed, but on average across the mixing layer they are not as diluted by air as lower Mach number experiments.

While these results provide new insight into mixing mechanisms and processes in shock-induced variable density flows, this work may also be particularly useful as a validation and calibration tool for turbulent mixing models and numerical simulations. The application of state of the art velocity and density field diagnostics allows quantitative comparisons of numerous flow field parameters, providing the opportunity for a rigorous approach to validation that extends far beyond previous studies that rely on mix width data and qualitative flow evolution.

[1] R. D. Richtmyer, "Taylor instability in shock acceleration of compressible fluids," Commun. Pure Appl. Math. **13**, 297–319 (1960).

[2] Y. Y. Meshkov, "Instability of a shock wave accelerated interface between two gases," Technical Report No. NASA TT F-13074 (NASA Technical Translation, 1970).

[3] M. Brouillette, "The Richtmyer-Meshkov instability," Annu. Rev. Fluid Mech. **34**, 445–468 (2002).

[4] P. Vorobieff and S. Kumar, "Experimental studies of Richtmyer-Meshkov instability," Recent Res. Dev. Fluid Dyn. **5**, 33–55 (2004).

[5] W. Hogan, R. Bangerter, and G. Kulcinski, "Energy from inertial fusion," Phys. Today **45**(9), 42–50 (1992).

[6] J. Lindl, "Development of the indirect-drive approach to inertial confinement fusion and the target physics basis for ignition and gain," Phys. Plasmas **2**, 3933–4024 (1995).

[7] J. Yang, T. Kubota, and E. E. Zukoski, "Applications of shock-induced mixing to supersonic combustion," AIAA J. **31**, 854–862 (1993).

[8] W. D. Arnett, J. N. Bahcall, R. P. Kirshner, and S. E. Woosley, "Supernova 1987a," Annu. Rev. Astron. Astrophys. **27**, 629–700 (1989).

[9] C. E. Niederhaus and J. W. Jacobs, "Experimental study of the Richtmyer-Meshkov instability of incompressible fluids," J. Fluid Mech. **485**, 243–277 (2003).

[10] X. Luo, X. Wang, and T. Si, "The Richtmyer-Meshkov instability of a three-dimensional air/SF_6 interface with a minimum-surface feature," J. Fluid Mech. **722**, R2-1–R2-11 (2013).

[11] S. Kumar, G. Orlicz, C. Tomkins, C. Goodenough, K. Prestridge, P. Vorobieff, and R. Benjamin, "Stretching of material lines in shock-accelerated gaseous flows," Phys. Fluids **17**, 082107 (2005).

[12] D. Ranjan, J. Niederhaus, B. Motl, M. Anderson, J. Oakley, and R. Bonazza, "Experimental investigation of primary and secondary features in high-Mach-number shock-bubble interaction," Phys. Rev. Lett. **98**, 024502 (2007).

[13] B. Motl, J. Oakley, D. Ranjan, C. Weber, M. Anderson, and R. Bonazza, "Experimental validation of a Richtmyer-Meshkov scaling law over large density ratio and shock strength ranges," Phys. Fluids **21**, 126102 (2009).

[14] G. C. Orlicz, B. J. Balakumar, C. D. Tomkins, and K. P. Prestridge, "A Mach number study of the Richtmyer-Meshkov instability in a varicose, heavy-gas curtain," Phys. Fluids **21**, 064102 (2009).

[15] C. Weber, A. Cook, and R. Bonazza, "Growth rate of a shocked mixing layer with known initial perturbations," J. Fluid Mech. **725**, 372–401 (2013).

[16] B. D. Collins and J. W. Jacobs, "PLIF flow visualization and measurements of the Richtmyer-Meshkov instability of an air/SF_6 interface," J. Fluid Mech. **464**, 113–136 (2002).

[17] C. Tomkins, S. Kumar, G. Orlicz, and K. Prestridge, "An experimental investigation of mixing mechanisms in shock-accelerated flow," J. Fluid Mech. **611**, 131–150 (2008).

[18] C. Weber, N. Haehn, J. Oakley, D. Rothamer, and R. Bonazza, "Turbulent mixing measurements in the Richtmyer-Meshkov instability," Phys. Fluids **24**, 074105 (2012).

[19] K. Prestridge, P. Vorobieff, P. M. Rightley, and R. F. Benjamin, "Validation of an instability growth model using particle image velocimetry measurements," Phys. Rev. Lett. **84**, 4353–4356 (2000).

[20] B. J. Balakumar, G. C. Orlicz, C. D. Tomkins, and K. P. Prestridge, "Simultaneous particle-image velocimetry-planar laser-induced fluorescence measurements of Richtmyer-Meshkov instability growth in a gas curtain with and without reshock," Phys. Fluids **20**, 124103 (2008).

[21] S. Balasubramanian, G. Orlicz, K. Prestridge, and B. Balakumar, "Experimental study of initial condition dependence on Richtmyer-Meshkov instability in the presence of reshock," Phys. Fluids **24**, 034103 (2012).

[22] P. E. Dimotakis, "Turbulent mixing," Annu. Rev. Fluid Mech. **37**, 329–356 (2005).

[23] J. W. Jacobs and V. V. Krivets, "Experiments on the late-time development of single-mode Richtmyer-Meshkov instability," Phys. Fluids **17**, 034105 (2005).

[24] D. Ranjan, M. Anderson, J. Oakley, and R. Bonazza, "Experimental investigation of a strongly shocked gas bubble," Phys. Rev. Lett. **94**, 184507 (2005).

[25] J. F. Haas and B. Sturtevant, "Interaction of weak shock waves with cylindrical and spherical gas inhomogeneities," J. Fluid Mech. **181**, 41–76 (1987).

[26] P. Vorobieff and M. Anderson, "Vortex formation in a shock-accelerated gas induced by particle seeding," Phys. Rev. Lett. **106**, 184503 (2011).

[27] K. O. Mikaelian, "Numerical simulations of Richtmyer-Meshkov instabilities in finite-thickness fluids layers," Phys. Fluids **8**, 1269–1292 (1996).

[28] L. M. Pickett and J. B. Ghandhi, "Passive scalar measurements in a planar mixing layer by PLIF of acetone," Exp. Fluids **31**, 309–318 (2001).

[29] H. Hughes, "Beer's law and the optimum transmittance in absorption measurements," Appl. Opt. **2**, 937–945 (1963).

[30] R. Reid, J. Prausnitz, and T. Sherwood, *The Properties of Gases and Liquids* (McGraw-Hill Book Company, New York, 1977), p. 411.

[31] M. Anderson, "Oblique shock interactions with perturbed density interfaces," Ph.D. thesis (University of New Mexico, 2011).

[32] D. Besnard, F. H. Harlow, R. M. Rauenzahn, and C. Zemach, "Turbulence transport equations for variable-density turbulence and their relationship to two-field models," Technical Report No. LA-12303-MS (Los Alamos National Laboratory, 1992).

[33] A. Cook and P. Dimotakis, "Transition stages of Rayleigh-Taylor instability between miscible fluids," J. Fluid Mech. **443**, 69–99 (2001).

[34] A. Cook, W. Cabot, and P. Miller, "The mixing transition in Rayleigh-Taylor instability," J. Fluid Mech. **511**, 333–362 (2004).

[35] D. Youngs, "Three-dimensional numerical simulation of turbulent mixing by Rayleigh-Taylor instability," Phys. Fluids **3**, 1312–1320 (1991).

[36] D. L. Youngs, "Numerical simulation of mixing by Rayleigh-Taylor and Richtmyer-Meshkov instabilities," Laser Part. Beams **12**, 725–750 (1994).

[37] M. Lombardini, D. Pullin, and D. Meiron, "Transition to turbulence in shock-driven mixing: A Mach number study," J. Fluid Mech. **690**, 203–226 (2012).

[38] K. Buch and W. Dahm, "Experimental study of the fine-scale structure of conserved scalar mixing in turbulent shear flows," J. Fluid Mech. **317**, 21–71 (1996).